Letter

Quantum interference tuning of spin-orbit coupling in twisted van der Waals trilayers

Csaba G. Péterfalvi,[1,*] Alessandro David,[2] Péter Rakyta,[3,4] Guido Burkard,[1,†] and Andor Kormányos[3,‡]

[1]*Department of Physics, University of Konstanz, D-78464 Konstanz, Germany*

[2]*Peter Grünberg Institute - Quantum Control (PGI-8), Forschungszentrum Jülich GmbH, Jülich, Germany*

[3]*Department of Physics of Complex Systems, Eötvös Loránd University, Budapest, Hungary*

[4]*Quantum Information National Laboratory, Hungary*

(Received 4 November 2021; revised 2 March 2022; accepted 9 March 2022; published 31 May 2022)

We show that in van der Waals stacks of twisted hexagonal layers the proximity induced Rashba spin-orbit coupling can be affected by quantum interference. We calculate the quantum phase responsible for this effect in graphene–transition metal dichalcogenide bilayers as a function of interlayer twist angle. We show how this quantum phase affects the spin polarization of the graphene bands and discuss its potential effect on spin-to-charge conversion measurements. In twisted trilayers symmetries can be broken as well as restored for certain twist angles. This can be used to deduce the effects of induced spin-orbit coupling on spin-lifetime anisotropy and magnetoconductance measurements.

DOI: 10.1103/PhysRevResearch.4.L022049

Multilayer stacks of two-dimensional (2D) materials, commonly referred to as van der Waals (vdW) heterostructures, have become an important platform for exploring a wide range of exciting phenomena, because they offer electronic tunability and a large parameter space. Initially, bilayer structures served as a platform to study, e.g., the effects of a moire potential in graphene/hBN [1–4], the induced spin-orbit coupling (SOC) in graphene/transition metal dichalcogenide (TMDC) heterostructures [5–7], or strong electronic correlations in magic-angle twisted bilayer graphene (MATG) [8,9]. A natural next step is to add another layer, which introduces a second twist angle and/or a further layer of different properties and this can enhance the parameter space to tune the properties of the system in several ways. An exciting opportunity is to use MATG and induce SOC into the flat bands by adding a TMDC layer to the stack [10,11]. Further examples include the recent proposal of an engineered topological phase in WSe_2/bilayer graphene (BLG)/WSe_2 system [12], the external gate tunability of SOC through changing layer polarization in TMDC/BLG structures [13–16], and imprinting double moiré potential on graphene [17–19]. More generally, vdW multilayers can serve as a quantum simulator platform for strongly correlated physics and topological materials [20].

The proximity induced SOC plays a pivotal role in many of the above proposals. A number of recent experimental works based on weak antilocalization (WAL) [5–7,21–25], spin-lifetime anisotropy measurements [26–29], spin-Hall [30–33], and Rashba-Edelstein effect [32,34–36] proved that SOC is strongly enhanced in graphene/TMDC heterostructures, which also motivated theoretical work to understand these measurements [5,37–44]. Recently, Refs. [45–48] have also discussed the interlayer twist angle dependence of the induced SOC in graphene/TMDC. In particular, it has been noted [46,47] that the most general form of the induced Rashba-SOC in twisted graphene/TMDC heterostructures that obeys time reversal $\mathcal{T}$ and threefold rotation C_3 symmetries can be written as

$$H_R = \frac{\lambda_R}{2} e^{i\frac{s_z}{2}\vartheta_R}(\tau_z\sigma_x s_y - \sigma_y s_x)e^{-i\frac{s_z}{2}\vartheta_R}, \tag{1}$$

where $s_{x,y,z}$ ($\sigma_{x,y,z}$) are Pauli matrices acting in the spin (sublattice) space, and τ_z is a Pauli matrix acting on the valley degree of freedom of graphene. Both ϑ_R and λ_R are functions of the interlayer twist angle θ, which we do not show explicitly in order to ease the notations. H_R differs from the usual Rashba SOC term [49–51] $H_R = \frac{\lambda_R}{2}(\tau_z\sigma_x s_y - \sigma_y s_x)$ by a rotation of angle ϑ_R in spin-space. The terms containing ϑ_R appear because for a general interlayer twist angle the symmetry of the heterostructure is lowered from C_{3v} to C_3. Thus, Eq. (1) is valid not only for graphene/TMDC heterostructures, but for a wide range of twisted heterostructures consisting of hexagonal layers, such as heterostructures of graphene with semiconductor [52,53], ferromagnetic [54], and topological insulator [55,56] structures. This general nature of the effect is one of the main motivations for our work. However, the physical significance of this spin-space rotation was not previously appreciated and the relation of ϑ_R to the interlayer twist angle θ has not been discussed. As we will show, using graphene/TMDC twisted bilayers as an example, ϑ_R can take finite values and it leads to quantum interference affecting the induced Rashba type SOC in twisted trilayers. While it has been known that λ_R is tunable, e.g., by pressure [57] in

*csaba.peterfalvi@uni-konstanz.de
†guido.burkard@uni-konstanz.de
‡andor.kormanyos@ttk.elte.hu

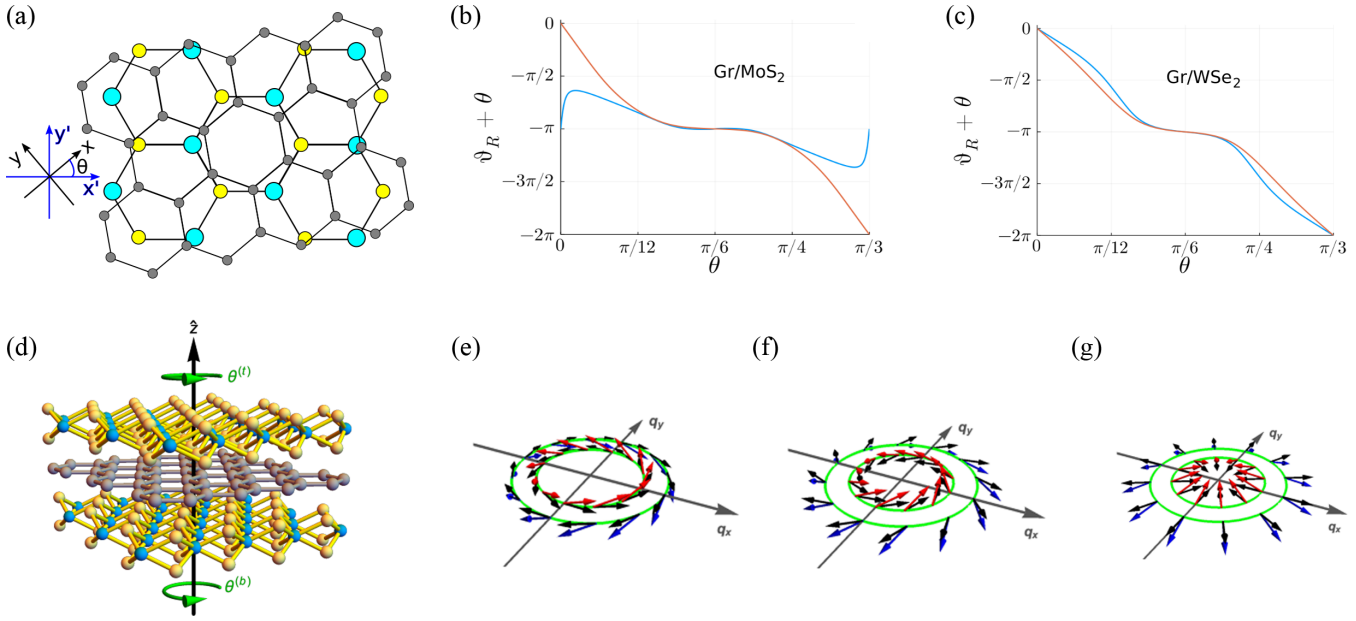

FIG. 1. (a) Schematics of a twisted graphene/TMDC bilayer with twist angle θ. (b) and (c) $\vartheta_R + \theta$ as a function of θ for MoS_2 and WSe_2. Blue (red) curves were calculated using DFT (ARPES measurements) parameters, see main text for details. (d) Schematics of a twisted TMDC/graphene/TMDC trilayer. The spin-orbit field $\mathbf{s}(\mathbf{q})$ for (e) $\theta = 0$, (f) $\theta = 7^\circ$, and (g) for $\theta = 15^\circ$, using the ϑ_R vs θ dependence shown in Fig. 1(c), calculated for graphene/WSe_2. The green circles indicate the Fermi surfaces for the two spin subbands. $\mathbf{s}(\mathbf{q})$ lies in the plane if only Rashba SOC is induced in graphene (black arrows), whereas it acquires a nonzero $\langle \hat{s}_z \rangle$ component if the valley Zeeman type SOC is finite as well (blue and red).

proximity structures, to our knowledge the possibility that quantum interference can affect its value has not been considered before.

Twisted bilayers. In order to obtain the angle ϑ_R, we use the methodology recently developed to calculate the coupling strength λ_R for graphene/TMDC bilayers [47]. ϑ_R is a quantum phase which depends on the interlayer tunneling between the Bloch states of graphene and the TMDC layer and on certain off-diagonal matrix elements of the intrinsic SOC of the TMDC, for details we refer to Ref. [58]. One finds that λ_R and ϑ_R are the absolute value and the phase of the complex Rashba coefficient $\bar{\lambda}_R = \lambda_R e^{i\vartheta_R}$, which is given by the sum of the contributions from pairs of even (e) and odd (o) bands of the TMDC: $\bar{\lambda}_R = \sum_q \lambda_{R,(e,o)_q} e^{i\vartheta_{(e,o)_q}} = \sum_q \lambda_{R,q} e^{i\vartheta_q}$. Here $\lambda_{R,q}$ and ϑ_q are the magnitude and the phase of the contributions of the pairs of bands. In the calculations of $\lambda_{R,q}$ and ϑ_q we have used the tight-binding model of Ref. [59]. For the initial steps of the calculations it is convenient to assume that the graphene layer is rotated with respect to the TMDC layer [47]. In the final steps we change the representation of the Hamiltonian from the coordinate system fixed to the TMDC layer to the system fixed to the graphene layer with a transformation $e^{-i\tau_z \frac{\sigma_z}{2}\theta} H_R e^{i\tau_z \frac{\sigma_z}{2}\theta}$, see Fig. 1(a). From the explicit form of the transformed Rashba Hamiltonian one finds that the nonzero matrix elements are $\propto \lambda_R e^{\pm i(\vartheta_R + \theta)}$, i.e., the sum of the geometric angle θ and the quantum phase ϑ_R plays an important role.

Regarding our numerical calculations, the first ingredient is the tight-binding (TB) Hamiltonian of Ref. [59] for TMDCs. This TB model itself is derived from density functional theory (DFT) calculations and we use it, among others, to calculate matrix elements of the spin-orbit coupling Hamiltonian and the interlayer tunneling amplitude. The results also depend on (i) the position of the Dirac point of graphene within the band gap E_g of the TMDC, and (ii) on the value of E_g. Numerical DFT calculations are known to often underestimate E_g and they seem to give [37] different results from experiments [60,61] for the energy alignment of graphene's Dirac point with the TMDC bands. We performed our calculations for two parameter sets to assess how sensitive are the results on the choice of these material parameters. Since Ref. [59] does not provide information on the band alignment of graphene and the TMDC layer, we use the DFT calculations of Ref. [37] for this purpose. The second parameter set for E_g and the band alignment is extracted from ARPES measurements [60,61]. Since the coupling between the layers is weak at the Dirac point of graphene, the band alignment should mainly depend on the work function difference between the two materials. Therefore, we assume that it does not depend on the interlayer twist angle. This is in agreement with the recent computational work of Ref. [62].

The results for the $\vartheta_R + \theta$ vs θ dependence for two selected TMDCs, MoS_2 and WSe_2, are shown in Figs. 1(b) and 1(c), respectively. In the case of MoS_2, using the DFT parameter set, one can see that $\vartheta_R + \theta$ remains in a limited range around π as θ varies from 0 to $\pi/3$ [Fig. 1(b)]. However, if parameters extracted from ARPES measurements [60] are used, then $\vartheta_R + \theta$ covers the entire range $[0, 2\pi]$. For WSe_2 one finds that $\vartheta_R + \theta$ covers all of $[0, 2\pi]$ [Fig. 1(c)] and the results obtained from the two parameter sets qualitatively agree. The difference between the results for the two materials can be mainly traced back to the different energy alignment of the Dirac point in the TMDC band gap. One can also note in Figs. 1(b) and 1(c) that for $\theta = l\pi/6$, $l = 0, 1, \ldots$ one

finds $\vartheta_R + \theta = n\pi$, where n is an integer. We give a detailed discussion of how this result for $\vartheta_R + \theta$ follows from our theoretical method in Ref. [58], but already note at this point that for $\theta = l\pi/6$ the vertical mirror planes of the graphene and the TMDC lattice line up and the system, as a whole, has C_{3v} symmetry. In this case the Hamiltonian of the induced Rashba SOC reads $H_R = (-1)^{n+1}\frac{\lambda_R(\theta)}{2}(\tau_z\sigma_x s_y - \sigma_y s_x)$, hence H_R simplifies to the form used previously in the literature [37,49]. We find that n can be, in general, both odd and even [see Figs. 1(b) and 1(c)], which means that $\lambda_R(\theta)$ can acquire a negative sign as θ is changed. Interestingly, when $\vartheta_R + \theta \neq n\pi$, the spin-orbit field $\mathbf{s}(\mathbf{q}) = (\langle\hat{s}_x\rangle, \langle\hat{s}_y\rangle, \langle\hat{s}_z\rangle)^T$ is not tangential to the Fermi surface as in the case of usual Rashba SOC [cf. Figs. 1(e)–1(g)]. Instead, one can show that the in-plane component $(\langle\hat{s}_x\rangle, \langle\hat{s}_y\rangle)^T$ is rotated by an angle $\vartheta_R + \theta$ with respect to the tangential direction. As we will discuss, this might have consequences on the interpretation of experimental results.

Twisted TMDC/graphene/TMDC trilayers. Adding another TMDC layer, as shown in Fig. 1(d), introduces a second interlayer twist angle and the two twist angles $\theta^{(b)}$ and $\theta^{(t)}$ for the bottom and top TMDC layers allow an even broader control of the induced SOC in graphene.

Since the layers are only weakly coupled, the effective graphene Hamiltonian is $H_{\rm orb} + H^{(t)}_{\rm soc} + H^{(b)}_{\rm soc}$, where $H^{(b)}_{\rm soc} = H^{(b)}_{\rm vZ} + H^{(b)}_R$ and $H^{(t)}_{\rm soc} = H^{(t)}_{\rm vZ} - H^{(t)}_R$. Here $H_{\rm vZ} = \lambda_{\rm vZ}\tau_z s_z$ is the Hamiltonian of the induced valley Zeeman SOC in the graphene layer. Note that the contributions $H^{(b)}_R$ and $H^{(t)}_R$ have a different sign. As a simple physical explanation, consider the case when the two TMDC layers are perfectly aligned, e.g., $\theta^{(b)} = \theta^{(t)}$. Then the graphene layer is a horizontal mirror plane of the whole stack, which dictates that the Rashba SOC must vanish. (A more microscopic argument is given in Ref. [58].) One can define the complex Rashba coefficient for the trilayer system (tls) by

$$\bar{\lambda}^{(\rm tls)}_R = \lambda^{(b)}_R e^{i(\vartheta^{(b)}_R + \theta^{(b)})} - \lambda^{(t)}_R e^{i(\vartheta^{(t)}_R + \theta^{(t)})}, \tag{2}$$

and its magnitude $\lambda^{(\rm tls)}_R = |\bar{\lambda}^{(\rm tls)}_R|$ and phase $\vartheta^{(\rm tls)} = {\rm Arg}[\bar{\lambda}^{(\rm tls)}_R]$. In terms of these quantities the induced Rashba type SOC can be written as $H^{(\rm tls)}_R = \frac{\lambda^{(\rm tls)}_R}{2} e^{i\frac{s_z}{2}\vartheta^{(\rm tls)}}(\tau_z\sigma_x s_y - \sigma_y s_x)e^{-i\frac{s_z}{2}\vartheta^{(\rm tls)}}$. The importance of the phase $e^{i(\vartheta_R+\theta)}$ discussed for bilayers becomes now more clear: it follows from Eq. (2) that the strength $\lambda^{(\rm tls)}_R$ of the induced Rashba SOC in trilayer stacks can be affected by quantum interference effects if $\vartheta^{(b)}_R + \theta^{(b)}$ and/or $\vartheta^{(t)}_R + \theta^{(t)}$ are nonzero. This can be interpreted as an interference of the virtual hopping processes to the two TMDC layers that give rise to the induced Rashba SOC. Calculations for the twist angle dependence of λ_R have already been performed in Refs. [46,47], therefore we do not show these results here, see Ref. [58] for further details. The results of our numerical calculations for $H^{(\rm tls)}_R$ are summarized in Figs. 2(a)–2(d). First, symmetries that are broken in bilayers can be restored in trilayers for certain $\theta^{(b)}$ and $\theta^{(t)}$ angles. If $|\theta^{(b)} - \theta^{(t)}| = l\pi/3$, where l is an odd integer, the trilayer stack is inversion symmetric. On the other hand, for an even l the stack has a horizontal mirror plane. Therefore the induced Rashba SOC must vanish for any integer l, as it can be seen in Figs. 2(a) and 2(b). For WSe_2 encapsulation [Fig. 2(a)] the

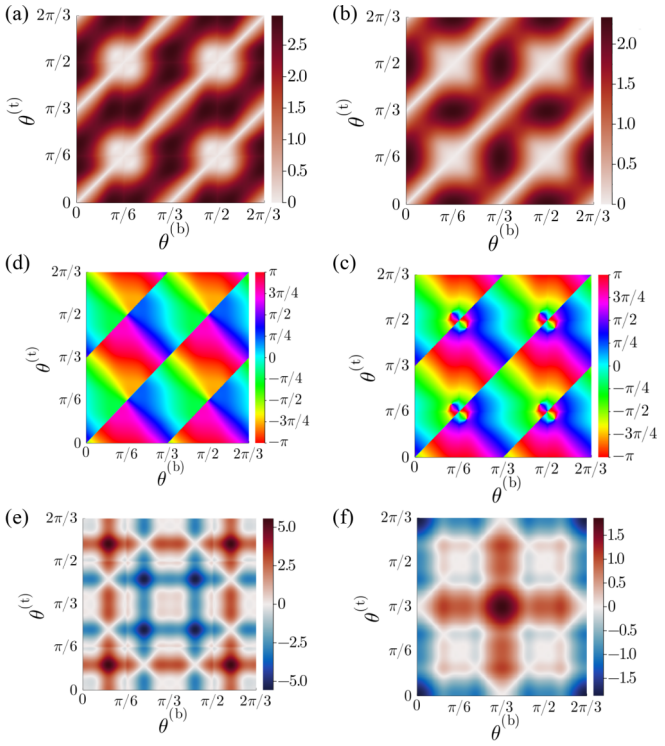

FIG. 2. (a) and (b) $\lambda^{(\rm tls)}_R$ for MoS_2 and WSe_2 two-sided encapsulation. (c) and (d) The angle $\vartheta^{(\rm tls)}$ for MoS_2 and WSe_2 two-sided encapsulation. (e) and (f) $\lambda^{(\rm tls)}_{\rm vZ}$ for MoS_2 and WSe_2 two-sided encapsulation. We used parameters from DFT band structure calculations, see [63].

maximum of $\lambda^{(\rm tls)}_R$ is found for $|\theta^{(b)} - \theta^{(t)}| = (2l+1)\pi/6$. The maximum value of $\lambda^{(\rm tls)}_R$ is around 70% larger than in the graphene/WSe_2 case. Thus, double-sided encapsulation can significantly enhance the induced Rashba SOC. Surprisingly, when using MoS_2 for double encapsulation [Fig. 2(b)], we find that $\lambda^{(\rm tls)}_R$ basically cannot be enhanced above the value obtained for one sided proximity effect. This can be understood by considering the explicit dependence of $\lambda^{(t,b)}_R$ and $\vartheta^{(t,b)}_R$ on $\theta^{(t,b)}$, see Ref. [58] for details. The origin of the extended regions where $\lambda^{(\rm tls)}_R$ is very small is due to the fact that for those twist angles λ_R and ϑ_R change slowly in both layers and therefore they approximately cancel in Eq. (2). In Figs. 2(c) and 2(d) we show the phase $\vartheta^{(\rm tls)}$ of Eq. (2), which determines the winding of the SOC field $\mathbf{s}(\mathbf{q})$ in the case of double encapsulation. The apparent diagonal lines correspond to $\lambda^{(\rm tls)}_R = 0$ where $\vartheta^{(\rm tls)}$ is not defined.

For completeness, we also discuss the twist angle dependence of the induced valley Zeeman SOC in TMDC/graphene/TMDC trilayers, see Figs. 2(e) and 2(f). The strength of the valley Zeeman type SOC is simply given by $\lambda^{(\rm tls)}_{\rm vZ} = \lambda^{(b)}_{\rm vZ}(\theta^{(b)}) + \lambda^{(t)}_{\rm vZ}(\theta^{(t)})$. If the two TMDC layers are (nearly) aligned, they can *double* the strength of the induced valley Zeeman SOC. When the whole stack has inversion symmetry, the effect of the two layers cancel and $\lambda^{(\rm tls)}_{\rm vZ} = 0$. The valley Zeeman SOC also vanishes along the lines $\theta^{(b)} + \theta^{(t)} = \pi/3, \pi$, this is a combined effect of time reversal and threefold rotation symmetry of the TMDC layers. We also

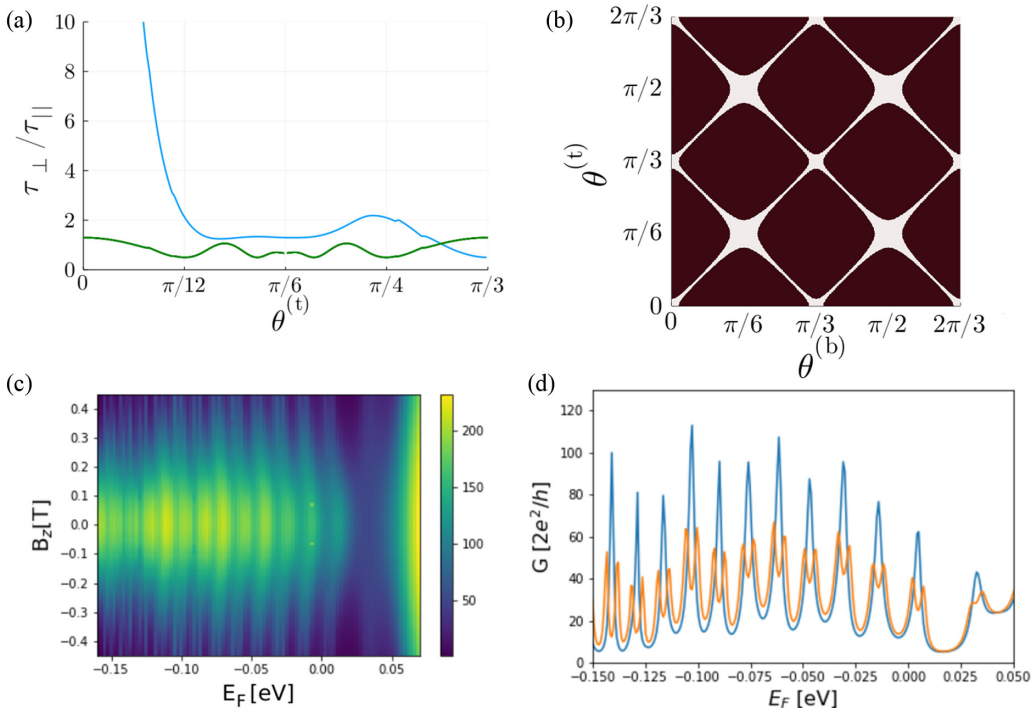

FIG. 3. (a) Calculated spin lifetime anisotropy in a TMDC/graphene/TMDC heterostructure as a function of $\theta^{(t)}$ for $\theta^{(b)} = 0^\circ$ (blue) and $\theta^{(b)} = 30^\circ$ (green). (b) White color indicates the regions in the $(\theta^{(t)}, \theta^{(b)})$ space where the REE is expected to vanish for a WSe_2/graphene/WSe_2 trilayer. In the calculations for (a) and (b) we used DFT parameters [63]. (c) Conductance G (in units of $2e^2/h$) through an *npn* junction as a function of magnetic field B_z and Fermi energy E_F for $\lambda_{vZ} = 2.6$ meV. (d) Cross section of (c) at fixed $B_z = 0.436$ T. $\lambda_{vZ} = 0$ meV (blue) and $\lambda_{vZ} = 2.6$ meV (orange).

note that $\lambda_{vZ}^{(tls)}$ depends sensitively on what kind of TMDC is used in the stacks. The difference between the effects of WSe_2 [Fig. 2(e)] and MoS_2 [Fig. 2(f)] is mainly due to the different alignment of graphene's Dirac point with the TMDC bands. The calculations shown in Fig. 2, together with Eq. (2), are the main results of this work.

In the preceding discussions of graphene/TMDC and TMDC/graphene/TMDC heterostructures we have neglected a possible lateral shift of the graphene layer with respect to the TMDCs and moiré effects. Regarding the lateral shift, it does not affect our results [58]. Considering the moiré effects, in graphene/TMDC bilayers they are present only at energy scales larger than 2 eV [58,60], i.e., they are negligible for energies close to the Dirac point of graphene. The situation might be different in TMDC/graphene/TMDC trilayers. Based on previous work of Refs. [64,65] on hBN/graphene/hBN trilayers, one may expect that supermoiré effects may become important when the TMDC layers are nearly aligned: $0 < |\theta^{(t)} - \theta^{(b)}| \lesssim 1^\circ$ (see Ref. [58] for further details). The discussion of supermoiré is beyond the scope of the present work.

Experimental predictions. Several recent works [26,28,29] measured an anisotropy of the out-of-plane $\tau_\perp$ and in-plane $\tau_\parallel$ spin lifetimes in graphene/TMDC heterostructures which can be interpreted as direct proof of induced SOC in graphene. Namely, according to the theoretical calculations of Ref. [39], if there is a strong intervalley scattering in graphene, then the ratio of the spin lifetimes is given by $\tau_\perp/\tau_\parallel = (\lambda_{vZ}/\lambda_R)^2(\tau_{iv}/\tau_p) + 1/2$, where τ_{iv} (τ_p) is the intervalley (momentum) scattering time. (For ultraclean samples with SOC comparable to or larger than the disorder-induced quasiparticle broadening, a qualitatively different spin relaxation anisotropy is derived in Ref. [66].) Let us consider a WSe_2/graphene/WSe_2 heterostructure and assume that $\theta^{(b)}$ is kept fixed while $\theta^{(t)}$ is changed. Note that the ratio λ_{vZ}/λ_R can be tuned in a wider range in trilayer structures than in bilayers. For example, λ_R is never zero for graphene/TMDC, whereas one can choose $\theta^{(b)}$ and $\theta^{(t)}$ such that $\lambda_{vZ}^{(tls)} \neq 0$ and $\lambda_R^{(tls)} = 0$, see Figs. 2(a) and 2(e). Using $\tau_{iv}/\tau_p \approx 5$ as in Ref. [39], we plot $\tau_\perp/\tau_\parallel$ as a function of $\theta^{(t)}$ for $\theta^{(b)} = 0^\circ$ and $\theta^{(b)} = 30^\circ$ in Fig. 3(a). When $\theta^{(b)} = 0$ and $1^\circ < \theta^{(t)} \lesssim 15^\circ$ then $\lambda_R^{(tls)}$ becomes small but $\lambda_{vZ}^{(tls)}$ is finite, therefore $\tau_\perp/\tau_\parallel$ strongly increases as a function of $\theta^{(t)}$. This enhancement happens before supermoiré effects might become important for $\theta^{(t)} \lesssim 1^\circ$. In contrast, if $\theta^{(b)} = 30^\circ$, then $\tau_\perp/\tau_\parallel$ remains finite for all $\theta^{(t)}$ angles. This dramatic difference in the $\theta^{(t)}$ dependence of $\tau_\perp/\tau_\parallel$ is clearly a consequence of the wider tunability of $\lambda_{vZ}^{(tls)}/\lambda_R^{(tls)}$ in trilayers.

One can expect that charge-to-spin conversion measurements should also be affected by the interlayer twist. Let us consider a graphene/TMDC bilayer and for simplicity assume that (i) $\lambda_{vZ} \ll \lambda_R$ and (ii) a DC electric field is applied along the $\hat{x}$ direction. In steady state the $\hat{y}$ component of the spin density is given by $\langle S_y \rangle = \frac{1}{2}\int \frac{d^2\mathbf{q}}{4\pi} s_y(\mathbf{q})\delta f_\mathbf{q}$ where $\delta f_\mathbf{q}$ is the deviation of the quasiparticle distribution with respect to equilibrium. Using the semiclassical argument given in Ref. [41], for Fermi energies close to the Dirac point E_D such that $|E_F - E_D| < \lambda_R(\theta)$, i.e., when there is a single Fermi sur-

face, one finds that $\langle S_y \rangle \propto \cos(\vartheta_R + \theta)$. This suggests that the Rashba-Edelstein effect (REE) may vanish [when $\vartheta_R + \theta = (2l+1)\pi/2$] even though $\lambda_R(\theta)$ is not required to be zero by symmetry for any θ. $\langle S_y \rangle$ can also change sign as a function of the interlayer twist angle, because $\vartheta_R + \theta \in [0, 2\pi]$, see Figs. 1(b) and 1(c). Regarding the more realistic situation when there are two spin-polarized Fermi surfaces in graphene for $|E_F - E_D| > \lambda_R$, looking at Fig. 1(g) one can understand that $\langle S_y \rangle$ can be zero as a function of twist angle in this case as well. Furthermore, in twisted TMDC/graphene/TMDC trilayers, the REE can vanish either because $\lambda_R^{(\mathrm{tls})} = 0$ or because $\vartheta^{(\mathrm{tls})} = (2l+1)\pi/2$, which can be expressed compactly as $\mathrm{Re}(\bar{\lambda}_R^{(\mathrm{tls})}) = 0$. As an example, the region where this condition is fulfilled in the $(\theta^{(t)}, \theta^{(b)})$ space for WSe_2/graphene/WSe_2 trilayers is shown in Fig. 3(b).

While the spin-lifetime anisotropy measurements require diffusive samples, in Figs. 3(c) and 3(d) we show an example of how strong SOC can affect ballistic transport properties. Highly transparent *np* and *npn* junctions in graphene have recently been realized in several experiments [67–71] and Fabry-Perrot type interference measurements [71]. Assume now that a TMDC/graphene/TMDC trilayer is tuned with interlayer twist angles such that the Rashba SOC is switched off and simultaneously the valley Zeeman SOC enhanced. We calculate the conductance [58] through a smooth graphene *npn* junction [72] as a function of out-of-plane magnetic field B_z and Fermi energy E_F for $\lambda_{vZ} = 2.6$ meV, see Fig. 3(c). One can observe that for $|B_z| > 0.3$ T the high-conductance ridges are split. This is apparent in Fig. 3(d), where we compare the cases when $\lambda_{vZ} = 0$ (blue) and $\lambda_{vZ} = 2.6$ meV (orange) for a fixed magnetic field $B_z = 0.436$ T. Our calculations also indicate that the Rashba type SOC does not have a similar effect on the conductance ridges (not shown). An additional experimental probe of the twist angle dependent SOC may be the measurement of the reflection of electrons at a planar junction, which is briefly discussed in Ref. [58].

Summary. We found that the induced Rashba type SOC in twisted hexagonal bilayers can be parametrized by the strength λ_R and a spin-rotation angle ϑ_R. This latter can lead to interference effects for λ_R in trilayer heterostructures. We also calculated the valley Zeeman SOC in twisted TMDC/graphene/TMDC trilayers. Finally, we discussed how the interlayer twist angle dependence of the induced SOC can be deduced from spin-lifetime anisotropy, charge-to-spin conversion, and magnetrotransport measurements.

In this work we have neglected possible lattice relaxation in vdW heterostructures [73]. An important future direction would be to study its effect on the results presented here.

Note added. During the preparation of this manuscript we have become aware of Ref. [62], where the authors discuss the twist angle dependence of the induced SOC in graphene/TMDC structures using DFT calculations.

Acknowledgments. We acknowledge helpful conversations with Péter Makk and Jaroslav Fabian. This research was supported by the Ministry of Innovation and Technology and the National Research, Development and Innovation Office (NKFIH) within the Quantum Information National Laboratory of Hungary. P.R. and A.K. were also supported by the ELTE Institutional Excellence Program (TKP2020-IKA-05), and the Hungarian Scientific Research Fund (OTKA) Grants No. K134437 and No. NN127903 (Topograph FlagERA project). A.K. acknowledges support from the Hungarian Academy of Sciences through the Bolyai János Stipendium (BO/00603/20/11) as well.

[1] M. Yankowitz, J. Xue, D. Cormode, J. D. Sanchez-Yamagishi, K. Watanabe, T. Taniguchi, P. Jarillo-Herrero, P. Jacquod, and B. J. LeRoy, Emergence of superlattice Dirac points in graphene on hexagonal boron nitride, Nat. Phys. **8**, 382 (2012).

[2] L. A. Ponomarenko, R. V. Gorbachev, G. L. Yu, D. C. Elias, R. Jalil, A. A. Patel, A. Mishchenko, A. S. Mayorov, C. R. Woods, J. R. Wallbank, M. Mucha-Kruczynski, B. A. Piot, M. Potemski, I. V. Grigorieva, K. S. Novoselov, F. Guinea, V. I. Fal'ko, and A. K. Geim, Cloning of Dirac fermions in graphene superlattices, Nature (London) **497**, 594 (2013).

[3] B. Hunt, J. D. Sanchez-Yamagishi, A. F. Young, M. Yankowitz, B. J. LeRoy, K. Watanabe, T. Taniguchi, P. Moon, M. Koshino, P. Jarillo-Herrero, and R. C. Ashoori, Massive Dirac fermions and Hofstadter butterfly in a van der Waals heterostructure, Science **340**, 1427 (2013).

[4] R. Ribeiro-Palau, C. Zhang, K. Watanabe, T. Taniguchi, J. Hone, and C. R. Dean, Twistable electronics with dynamically rotatable heterostructures, Science **361**, 690 (2018).

[5] Z. Wang, D.-K. Ki, H. Chen, H. Berger, A. H. MacDonald, and A. F. Morpurgo, Strong interface-induced spin-orbit interaction in graphene on WS_2, Nat. Commun. **6**, 8339 (2015).

[6] Z. Wang, D.-K. Ki, J. Y. Khoo, D. Mauro, H. Berger, L. S. Levitov, and A. F. Morpurgo, Origin and Magnitude of 'Designer' Spin-Orbit Interaction in Graphene on Semiconducting Transition Metal Dichalcogenides, Phys. Rev. X **6**, 041020 (2016).

[7] B. Yang, M.-F. Tu, J. Kim, Y. Wu, H. Wang, J. Alicea, R. Wu, M. Bockrath, and J. Shi, Tunable spin-orbit coupling and symmetry-protected edge states in graphene/WS_2, 2D Mater. **3**, 031012 (2016).

[8] R. Bistritzer and A. H. MacDonald, Moiré bands in twisted double-layer graphene, Proc. Natl. Acad. Sci. USA **108**, 12233 (2011).

[9] Y. Cao, V. Fatemi, S. Fang, K. Watanabe, T. Taniguchi, E. Kaxiras, and P. Jarillo-Herrero, Unconventional superconductivity in magic-angle graphene superlattices, Nature (London) **556**, 43 (2018).

[10] H. S. Arora, R. Polski, Y. Zhang, A. Thomson, Y. Choi, H. Kim, Z. Lin, I. Z. Wilson, X. Xu, J.-H. Chu, K. Watanabe, T. Taniguchi, J. Alicea, and S. Nadj-Perge, Superconductivity in metallic twisted bilayer graphene stabilized by WSe_2, Nature (London) **583**, 379 (2020).

[11] J.-X. Lin, Y.-H. Zhang, E. Morissette, Z. Wang, S. Liu, D. Rhodes, K. Watanabe, T. Taniguchi, J. Hone, and J. I. A. Li, Spin-orbit-driven ferromagnetism at half moiré filling in magic-angle twisted bilayer graphene, Science **375**, 437 (2022).

[12] J. O. Island, X. Cui, C. Lewandowski, J. Y. Khoo, E. M. Spanton, H. Zhou, D. Rhodes, J. C. Hone, T. Taniguchi, K. Watanabe, L. S. Levitov, M. P. Zaletel, and A. F. Young, Spin–orbit-driven band inversion in bilayer graphene by the van der Waals proximity effect, Nature (London) **571**, 85 (2019).

[13] J. Y. Khoo, A. F. Morpurgo, and L. Levitov, On-demand spin-orbit interaction from which-layer tunability in bilayer graphene, Nano Lett. **17**, 7003 (2017).

[14] M. Gmitra and J. Fabian, Proximity Effects in Bilayer Graphene on Monolayer WSe_2: Field-Effect Spin Valley Locking, Spin-Orbit Valve, and Spin Transistor, Phys. Rev. Lett. **119**, 146401 (2017).

[15] D. Wang, S. Che, G. Cao, R. Lyu, K. Watanabe, T. Taniguchi, C. N. Lau, and M. Bockrath, Quantum Hall effect measurement of spin-orbit coupling strengths in ultraclean bilayer graphene/WSe_2 heterostructures, Nano Lett. **19**, 7028 (2019).

[16] P. Tiwari, S. K. Srivastav, and A. Bid, Electric-Field-Tunable Valley Zeeman Effect in Bilayer Graphene Heterostructures: Realization of the Spin-Orbit Valve Effect, Phys. Rev. Lett. **126**, 096801 (2021).

[17] Z. Wang, Y. B. Wang, J. Yin, E. Tóvári, Y. Yang, L. Lin, M. Holwill, J. Birkbeck, D. J. Perello, S. Xu, J. Zultak, R. V. Gorbachev, A.V. Kretinin, T. Taniguchi, K. Watanabe, S. V. Morozov, M. Andjelković, S.P. Milovanović, L. Covaci, F. M. Peeters *et al.*, Composite super-moiré lattices in double-aligned graphene heterostructures, Sci. Adv. **5**, eaay8897 (2019).

[18] Z. Zhu, P. Cazeaux, M. Luskin, and E. Kaxiras, Modeling mechanical relaxation in incommensurate trilayer van der Waals heterostructures, Phys. Rev. B **101**, 224107 (2020).

[19] L. Wang, S. Zihlmann, M.-H. Liu, P. Makk, K. Watanabe, T. Taniguchi, A. Baumgartner, and C. Schönenberger, New generation of moiré superlattices in doubly aligned hBN/graphene/hBN heterostructures, Nano Lett. **19**, 2371 (2019).

[20] D. M. Kennes, M. Claassen, L. Xian, A. Georges, A. J. Millis, J. Hone, C. R. Dean, D. N. Basov, A. N. Pasupathy, and A. Rubio, Moiré heterostructures as a condensed-matter quantum simulator, Nat. Phys. **17**, 155 (2021).

[21] B. Yang, M. Lohmann, D. Barroso, I. Liao, Z. Lin, Y. Liu, L. Bartels, K. Watanabe, T. Taniguchi, and J. Shi, Strong electron-hole symmetric Rashba spin-orbit coupling in graphene/monolayer transition metal dichalcogenide heterostructures, Phys. Rev. B **96**, 041409(R) (2017).

[22] T. Völkl, T. Rockinger, M. Drienovsky, K. Watanabe, T. Taniguchi, D. Weiss, and J. Eroms, Magnetotransport in heterostructures of transition metal dichalcogenides and graphene, Phys. Rev. B **96**, 125405 (2017).

[23] S. Zihlmann, A. W. Cummings, J. H. Garcia, M. Kedves, K. Watanabe, T. Taniguchi, C. Schönenberger, and P. Makk, Large spin relaxation anisotropy and valley-Zeeman spin-orbit coupling in WSe_2/graphene/hBN heterostructures, Phys. Rev. B **97**, 075434 (2018).

[24] T. Wakamura, F. Reale, P. Palczynski, S. Guéron, C. Mattevi, and H. Bouchiat, Strong Anisotropic Spin-Orbit Interaction Induced in Graphene by Monolayer WS_2, Phys. Rev. Lett. **120**, 106802 (2018).

[25] T. Wakamura, F. Reale, P. Palczynski, M. Q. Zhao, A. T. C. Johnson, S. Guéron, C. Mattevi, A. Ouerghi, and H. Bouchiat, Spin-orbit interaction induced in graphene by transition metal dichalcogenides, Phys. Rev. B **99**, 245402 (2019).

[26] T. S. Ghiasi, J. Ingla-Aynés, A. A. Kaverzin, and B. J. van Wees, Large proximity-induced spin lifetime anisotropy in transition-metal dichalcogenide/graphene heterostructures, Nano Lett. **17**, 7528 (2017).

[27] J. C. Leutenantsmeyer, J. Ingla-Aynés, J. Fabian, and B. J. van Wees, Observation of Spin-Valley-Coupling-Induced Large Spin-Lifetime Anisotropy in Bilayer Graphene, Phys. Rev. Lett. **121**, 127702 (2018).

[28] L. A. Benítez, J. F. Sierra, W. S. Torres, A. Arrighi, F. Bonell, M. V. Costache, and S. O. Valenzuela, Strongly anisotropic spin relaxation in graphene-transition metal dichalcogenide heterostructures at room temperature, Nat. Phys. **14**, 303 (2018).

[29] J. Xu, T. Zhu, Y. K. Luo, Y.-M. Lu, and R. K. Kawakami, Strong and Tunable Spin-Lifetime Anisotropy in Dual-Gated Bilayer Graphene, Phys. Rev. Lett. **121**, 127703 (2018).

[30] C. K. Safeer, J. Ingla-Aynés, F. Herling, J. H. Garcia, M. Vila, N. Ontoso, M. R. Calvo, S. Roche, L. E. Hueso, and F. Casanova, Room-temperature spin Hall effect in graphene/MoS_2 van der Waals heterostructures, Nano Lett. **19**, 1074 (2019).

[31] F. Herling, C. K. Safeer, J. Ingla-Aynés, N. Ontoso, L. E. Hueso, and F. Casanova, Gate tunability of highly efficient spin-to-charge conversion by spin Hall effect in graphene proximitized with WSe_2, APL Mater. **8**, 071103 (2020).

[32] L. A. Benítez, W. Savero Torres, J. F. Sierra, M. Timmermans, J. H. Garcia, S. Roche, M. V. Costache, and S. O. Valenzuela, Tunable room-temperature spin galvanic and spin Hall effects in van der Waals heterostructures, Nat. Mater. **19**, 170 (2020).

[33] A. Md. Hoque, D. Khokhriakov, B. Karpiak, and S. P. Dash, Charge-spin conversion in layered semimetal $TaTe_2$ and spin injection in van der Waals heterostructures, Phys. Rev. Res. **2**, 033204 (2020).

[34] T. S. Ghiasi, A. A. Kaverzin, P. J. Blah, and B. J. van Wees, Charge-to-spin conversion by the Rashba-Edelstein effect in two-dimensional van der Waals heterostructures up to room temperature, Nano Lett. **19**, 5959 (2019).

[35] D. Khokhriakov, A. Md. Hoque, B. Karpiak, and S. P. Dash, Gate-tunable spin-galvanic effect in graphene-topological insulator van der Waals heterostructures at room temperature, Nat. Commun. **11**, 3657 (2020).

[36] L. Li, J. Zhang, G. Myeong, W. Shin, H. Lim, B. Kim, S. Kim, T. Jin, S. Cavill, B. S. Kim, C. Kim, J. Lischner, A. Ferreira, and S. Cho, Gate-tunable reversible Rashba-Edelstein effect in a few-layer graphene/2H-TaS_2 heterostructure at room temperature, ACS Nano **14**, 5251 (2020).

[37] M. Gmitra, D. Kochan, P. Högl, and J. Fabian, Trivial and inverted Dirac bands and the emergence of quantum spin Hall states in graphene on transition-metal dichalcogenides, Phys. Rev. B **93**, 155104 (2016).

[38] M. Milletari, M. Offidani, A. Ferreira, and R. Raimondi, Covariant Conservation Laws and the Spin Hall Effect in Dirac-Rashba Systems, Phys. Rev. Lett. **119**, 246801 (2017).

[39] A. W. Cummings, J. H. Garcia, J. Fabian, and S. Roche, Giant Spin Lifetime Anisotropy in Graphene Induced by Proximity Effects, Phys. Rev. Lett. **119**, 206601 (2017).

[40] J. H. Garcia, A. W. Cummings, and S. Roche, Spin Hall effect and weak antilocalization in graphene/transition metal dichalcogenide heterostructures, Nano Lett. **17**, 5078 (2017).

[41] M. Offidani, M. Milletari, R. Raimondi, and A. Ferreira, Optimal Charge-to-Spin Conversion in Graphene on Transition-

Metal Dichalcogenides, Phys. Rev. Lett. **119**, 196801 (2017).

[42] J. H. Garcia, M. Vila, A. W. Cummings, and S. Roche, Spin transport in graphene/transition metal dichalcogenide heterostructures, Chem. Soc. Rev. **47**, 3359 (2018).

[43] Y. S. Gani, E. J. Walter, and E. Rossi, Proximity-induced spin-orbit splitting in graphene nanoribbons on transition-metal dichalcogenides, Phys. Rev. B **101**, 195416 (2020).

[44] S. A. Cavill, C. Huang, M. Offidani, Y.-H. Lin, M. A. Cazalilla, and A. Ferreira, Proposal for Unambiguous Electrical Detection of Spin-Charge Conversion in Lateral Spin Valves, Phys. Rev. Lett. **124**, 236803 (2020).

[45] A. M. Alsharari, M. M. Asmar, and S. E. Ulloa, Topological phases and twisting of graphene on a dichalcogenide monolayer, Phys. Rev. B **98**, 195129 (2018).

[46] Y. Li and M. Koshino, Twist-angle dependence of the proximity spin-orbit coupling in graphene on transition-metal dichalcogenides, Phys. Rev. B **99**, 075438 (2019).

[47] A. David, P. Rakyta, A. Kormányos, and G. Burkard, Induced spin-orbit coupling in twisted graphene–transition metal dichalcogenide heterobilayers: Twistronics meets spintronics, Phys. Rev. B **100**, 085412 (2019).

[48] A. Pezo, Z. Zanolli, N. Wittemeier, P. Ordejón, A. Fazzio, S. Roche, and J. H. Garcia, Manipulation of spin transport in graphene/transition metal dichalcogenide heterobilayers upon twisting, 2D Mater. **9**, 015008 (2022).

[49] C. L. Kane and E. J. Mele, Quantum Spin Hall Effect in Graphene, Phys. Rev. Lett. **95**, 226801 (2005).

[50] H. Min, J. E. Hill, N. A. Sinitsyn, B. R. Sahu, L. Kleinman, and A. H. MacDonald, Intrinsic and Rashba spin-orbit interactions in graphene sheets, Phys. Rev. B **74**, 165310 (2006).

[51] S. Konschuh, M. Gmitra, and J. Fabian, Tight-binding theory of the spin-orbit coupling in graphene, Phys. Rev. B **82**, 245412 (2010).

[52] K. Zollner, A. W. Cummings, S. Roche, and J. Fabian, Graphene on two-dimensional hexagonal BN, AlN, and GaN: Electronic, spin-orbit, and spin relaxation properties, Phys. Rev. B **103**, 075129 (2021).

[53] X. Yang, B. Sa, P. Lin, C. Xu, Q. Zhu, H. Zhan, and Z. Sun, Tunable contacts in graphene/InSe van der Waals heterostructures, J. Phys. Chem. C **124**, 23699 (2020).

[54] K. Zollner, M. D. Petrović, K. Dolui, P. Plecháč, B. K. Nikolić, and J. Fabian, Scattering-induced and highly tunable by gate damping-like spin-orbit torque in graphene doubly proximitized by two-dimensional magnet $Cr_2Ge_2Te_6$ and monolayer WS_2, Phys. Rev. Res. **2**, 043057 (2020).

[55] K. Zollner and J. Fabian, Single and bilayer graphene on the topological insulator Bi_2Se_3: Electronic and spin-orbit properties from first principles, Phys. Rev. B **100**, 165141 (2019).

[56] K. Kandrai, P. Vancsó, G. Kukucska, J. Koltai, G. Baranka, Á. Hoffmann, Á. Pekker, K. Kamarás, Z. E. Horváth, A. Vymazalová, L. Tapasztó, and P. Nemes-Incze, Signature of large-gap quantum spin hall state in the layered mineral jacutingaite, Nano Lett. **20**, 5207 (2020).

[57] B. Fülöp, A. Márffy, S. Zihlmann, M. Gmitra, E. Tóvári, B. Szentpéteri, M. Kedves, K. Watanabe, T. Taniguchi, J. Fabian, C. Schönenberger, P. Makk, and S. Csonka, Boosting proximity spin–orbit coupling in graphene/WSe_2 heterostructures via hydrostatic pressure, npj 2D Mater. Appl. **5**, 82 (2021).

[58] See Supplemental Material at http://link.aps.org/supplemental/10.1103/PhysRevResearch.4.L022049 for (i) discussion of the symmetry properties of the quantum phase ϑ_R, (ii) details of the numerical calculations shown in Figs. 1–2, (iii) brief discussion of supermoire effects, (iv) details of the magnetotransport calculations shown in Fig. 3, (v) brief discussion of another setup to investigate twist angle dependent transport in a graphene-TMDC heterostructure.

[59] S. Fang, R. Kuate Defo, S. N. Shirodkar, S. Lieu, G. A. Tritsaris, and E. Kaxiras, *Ab initio* tight-binding Hamiltonian for transition metal dichalcogenides, Phys. Rev. B **92**, 205108 (2015).

[60] D. Pierucci, H. Henck, J. Avila, A. Balan, C. H. Naylor, G. Patriarche, Y. J. Dappe, M. G. Silly, F. Sirotti, A. T. C. Johnson, M. C. Asensio, and A. Ouerghi, Band alignment and minigaps in monolayer MoS_2-graphene van der Waals heterostructures, Nano Lett. **16**, 4054 (2016).

[61] H. Nakamura, A. Mohammed, Ph. Rosenzweig, K. Matsuda, K. Nowakowski, K. Küster, P. Wochner, S. Ibrahimkutty, U. Wedig, H. Hussain, J. Rawle, C. Nicklin, B. Stuhlhofer, G. Cristiani, G. Logvenov, H. Takagi, and U. Starke, Spin splitting and strain in epitaxial monolayer WSe_2 on graphene, Phys. Rev. B **101**, 165103 (2020).

[62] T. Naimer, K. Zollner, M. Gmitra, and J. Fabian, Twist-angle dependent proximity induced spin-orbit coupling in graphene/transition metal dichalcogenide heterostructures, Phys. Rev. B **104**, 195156 (2021).

[63] We describe the energy of the Dirac point of graphene in the band gap of the TMDC by a number $f_G \in [0, 1]$. Its value is a linear function of the position of the Dirac point in the TMDC band gap. When $f_G = 0$, the Dirac point is aligned with the TMDC valence band edge, for $f_G = 1$ the Dirac point has the same energy as the TMDC conduction band edge. In the calculations involving MoS_2, we used DFT parameters $E_g = 1.807$ eV, $f_G = 0.974$ and experimental parameters [60] $E_g = 2$ eV, $f_G = 0.55$. In the case of WSe_2, DFT parameters were $E_g = 1.638$ eV, $f_G = 0.161$ and experimental ones [61] $E_g = 1.95$ eV, $f_G = 0.426$.

[64] M. Andjelković, S. P. Milovanović, L. Covaci, and F. M. Peeters, Double moiré with a twist: Supermoiré in encapsulated graphene, Nano Lett. **20**, 979 (2020).

[65] H. Oka and M. Koshino, Fractal energy gaps and topological invariants in hBN/graphene/hBN double moiré systems, Phys. Rev. B **104**, 035306 (2021).

[66] M. Offidani and A. Ferreira, Microscopic theory of spin relaxation anisotropy in graphene with proximity-induced spin-orbit coupling, Phys. Rev. B **98**, 245408 (2018).

[67] A. F. Young and P. Kim, Quantum interference and Klein tunnelling in graphene heterojunctions, Nat. Phys. **5**, 222 (2009).

[68] P. Rickhaus, R. Maurand, M.-H. Liu, M. Weiss, K. Richter, and C. Schönenberger, Ballistic interferences in suspended graphene, Nat. Commun. **4**, 2342 (2013).

[69] P. Rickhaus, P. Makk, M.-H. Liu, E. Tóvári, M. Weiss, R. Maurand, K. Richter, and C. Schönenberger, Snake trajectories in ultraclean graphene p–n junctions, Nat. Commun. **6**, 6470 (2015).

[70] S. Chen, Z. Han, M. M. Elahi, K. M. Masum Habib, L. Wang, B. Wen, Y. Gao, T. Taniguchi, K. Watanabe, J. Hone, A. W. Ghosh, and C. R. Dean, Electron optics with p-n junctions in ballistic graphene, Science **353**, 1522 (2016).

[71] C. Handschin, P. Makk, P. Rickhaus, M.-H. Liu, K. Watanabe, T. Taniguchi, K. Richter, and C. Schönenberger, Fabry-Perot resonances in a graphene/hBN moiré superlattice, Nano Lett. **17**, 328 (2017).

[72] A. V. Shytov, M. S. Rudner, and L. S. Levitov, Klein Backscattering and Fabry-Pérot Interference in Graphene Heterojunctions, Phys. Rev. Lett. **101**, 156804 (2008).

[73] A. Silva, V. E. P. Claerbout, T. Polcar, D. Kramer, and P. Nicolini, Exploring the stability of twisted van der Waals heterostructures, ACS Appl. Mater. Interfaces **12**, 45214 (2020).

Supplementary information to the paper "Quantum interference tuning of spin-orbit coupling in twisted van der Waals trilayers"

Csaba G. Péterfalvi,[1] Alessandro David,[2] Péter Rakyta,[3,4] Guido Burkard,[1] and Andor Kormányos[3]

[1] *Department of Physics, University of Konstanz, D-78464 Konstanz, Germany*
[2] *Peter Grünberg Institute - Quantum Control (PGI-8), Forschungszentrum Jülich GmbH, Jülich, Germany*
[3] *Department of Physics of Complex Systems, Eötvös Loránd University, Budapest, Hungary*
[4] *Quantum Information National Laboratory, Hungary*

I. SYMMETRY PROPERTIES OF THE PHASE ϑ_R

In order to be self-contained and to set the stage, in Sec. I A and I B we carefully re-derive previous results of Ref. [1] for the Hamiltonian H_R^{gr}, which describes the proximity induced Rashba SOC in graphene. We then present two short, but important discussions. First, in Sec. I C we argue that the sign of the SOC coupling λ_R depends on the layer stacking order and this is important in trilayer stacks. Next, in Sec. I D we discuss the effects of the interlayer twist on H_R^{gr}. Our most important results in this section follow in Sec. I E. We prove that the results for the quantum phase ϑ_R simplify for interlayer twist angles $\theta = 0, \pi/6, \pi/3$, where the bilayer stack has C_{3v} symmetry. Finally, in Sec. I F we give a further discussion of the results obtained in Sec. I E.

A. Preliminaries

1. Lattice vectors

Both graphene and the TMDC layer have hexagonal lattices. We define the lattice vectors $\mathbf{a}_1 = \frac{a}{2}\left(1,\sqrt{3}\right)^T$, $\mathbf{a}_2 = \frac{a}{2}\left(1,-\sqrt{3}\right))^T$ (see Fig. 1(a)) and the corresponding primitive reciprocal lattice vectors $\mathbf{b}_1 = \frac{2\pi}{a}\left(1,1/\sqrt{3}\right)^T$, $\mathbf{b}_2 = \frac{2\pi}{a}\left(1,-1/\sqrt{3}\right))^T$. Here $a = a_{gr}$ ($a = a_{tmdc}$) is the lattice constant for graphene (TMDC). We will distinguish the reciprocal lattice vectors $\mathbf{b}_{1,2}$ of graphene from the TMDC ones by using the notation $\mathbf{b}'_{1,2}$ for the latter. The position of the A and B sublattice in the unit cell is given by $\mathbf{t}_A = \frac{a_{gr}}{2}\left(1,1/\sqrt{3}\right)^T$, $\mathbf{t}_B = \frac{a_{gr}}{2}\left(1,-1/\sqrt{3}\right)^T$. The metal (chalcogen) atoms occupy a position corresponding to the A (B) sublattice in the unit cell of the TMDC.

2. Formalism to calculate the induced SOC

As it was shown in Ref[1], an important contribution to the proximity induced Bychkov-Rashba type SOC in graphene comes from virtual interlayer tunneling processes to the TMDC layer. In third order perturbation theory it is given by

$$(H_R^{gr})_{Xs,X's'} = \sum_{j,b,b',s'',s'''} \frac{\left(T(\tau\mathbf{k}'_j)\right)_{Xs,bs''}\left(H_{\rm soc}\right)_{bs'',b's'''}\left(T^\dagger(\tau\mathbf{k}'_j)\right)_{b's''',X's'}}{[E_D^{\rm gr} - E_b^{\rm tmdc}(\tau\mathbf{k}'_j)][E_D^{\rm gr} - E_{b'}^{\rm tmdc}(\tau\mathbf{k}'_j)]}. \tag{1}$$

Here $X = \{A, B\}$ runs over sublattice indices of graphene, s, s' are spin indices and $b \neq b'$ are band indices running over the bands of the (isolated) TMDC layer. Spin-flip process can be facilitated by certain off-diagonal elements of the intrinsic SOC matrix of the monolayer TMDC denoted by $(H_{\rm soc})_{bs,b's'}$ The spin-flip off-diagonal matrix elements are allowed between pairs of bands b, b' if one of the bands is symmetric (even) and the other one is antisymmetric (odd) with respect to reflection on the horizontal mirror plane of the TMDC (see, e.g., Ref. [2] for further discussion of the SOC in monolayer TMDCs).

We assume that the graphene layer is rotated with respect to the TMDC layer by a twist angle θ. Therefore, as indicated in Fig. 1(b), the BZ of graphene is also rotated. For each interlayer twist angle θ the right-hand side of Eq. (1) needs to be evaluated for wavenumbers $\tau\mathbf{k}'_j$ in the TMDC Brillouin zone (see Fig. 1(b)) that are determined by quasimomentum conservation condition $\tau\mathbf{K}^\theta + \mathbf{G}^\theta = \mathbf{k}' + \mathbf{G}'$, such that $|\tau\mathbf{K}^\theta + \mathbf{G}^\theta| = |\mathbf{K}^\theta|$. Here $\tau\mathbf{K}^\theta$, $\tau = \pm 1$ denote the wavevector to the Dirac point of graphene and $\mathbf{G}^\theta$ and ($\mathbf{G}'$) are reciprocal lattice vectors of graphene (TMDC). As indicated in Fig. 1(b), for each $\tau\mathbf{K}^\theta$ there are three wavevectors $\tau\mathbf{k}'_j$ and corresponding reciprocal lattice vectors $\mathbf{G}_j^\theta$ and $\mathbf{G}'_j$ that satisfy the quasimomentum conservation condition. These $\tau\mathbf{k}'_j$ vectors are related by $2\pi/3$ rotations. Explicitly, one finds $\mathbf{G}^\theta_{1,2,3} = -\mathbf{b}^\theta_2, -\mathbf{b}^\theta_1, 0$ and $\mathbf{G}'_{1,2,3} = -\mathbf{b}'_2, -(\mathbf{b}'_1 - \mathbf{b}'_2), \mathbf{b}'_1$. $E_b^{\rm tmdc}(\tau\mathbf{k}'_j)$ denote TMDC bands energies and $E_D^{\rm gr}$ is the energy of the Dirac point of graphene. $(T_{\tau\mathbf{k}'_j})_{Xs,bs''}$ is the tunneling matrix between Bloch states at $\tau\mathbf{K}^\theta$ to states at $\tau\mathbf{k}'_j$. We assume spin-independent tunneling and therefore $(T_{\tau\mathbf{k}'_j})_{Xs,bs''}$ is diagonal in the spin space. $(T_{\tau\mathbf{k}'_j})_{Xs,bs''}$ can be written as

$$\left(T(\tau\boldsymbol{k}'_j)\right)_{Xb} = \langle\Psi^{(X)}_{gr}(\mathbf{K}^\theta_1, \mathbf{r})|H_{orb}|\Psi^{(b)}_{tmdc}(\mathbf{k}'_j, \mathbf{r})\rangle = e^{i\tau\boldsymbol{G}^\theta_j\cdot\boldsymbol{d}_0} t_b(\tau\mathbf{k}'_j) e^{i\tau\phi_j^X} \tag{2}$$

Here H_{orb} is the orbital part of the Hamiltonian of the system (without the SOC), $\Psi^{(X)}_{gr}(\mathbf{K}^{\theta}_1,\mathbf{r})$ and $\Psi^{(b)}_{tmdc}(\mathbf{k}'_j,\mathbf{r})$ are Bloch wavefunctions of graphene and of band b of the TMDC layer, respectively. A possible lateral shift of the graphene lattice with respect to the TMDC lattice is denoted by $\mathbf{d}_0$. The phase ϕ^X_j is defined as $\phi^X_j = \boldsymbol{t}_X \cdot \mathbf{G}_j$. The tunneling amplitude $t_b(\tau\mathbf{k}'_j)$ to band b of the TMDC can be written as

$$t_b(\tau\mathbf{k}'_j) = e^{-i\tau\boldsymbol{G}'_j\cdot\boldsymbol{t}'_X} t^p_b\left(\tau\mathbf{k}'_j\right) + e^{-i\tau\boldsymbol{G}'_j\cdot\boldsymbol{t}'_{X'}} t^d_b\left(\tau\mathbf{k}'_j\right), \tag{3}$$

where $\boldsymbol{t}'_X$ ($\boldsymbol{t}'_{X'}$), $X \neq X'$ is the vector pointing to the chalcogen (metal) atom position in the unit cell of the TMDC layer, and $t^p_b(\tau\mathbf{k}'_j)$ ($t^d_b((\tau\mathbf{k}'_j)$) describes the interlayer tunneling between graphene and the p orbitals of the chalcogen (d orbitals of the metal) atoms. The calculation of the amplitude $t^{p,d}_b(\tau\mathbf{k}'_1)$ in terms of materials dependent parameters will be discussed in Sec. II A.

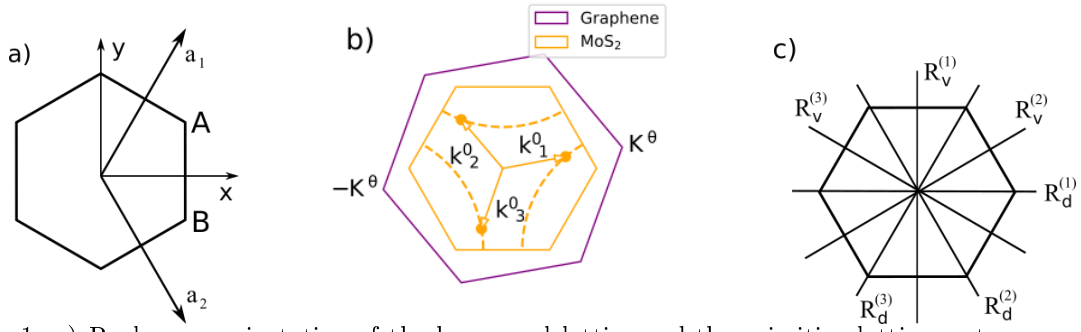

FIG. 1: a) Real space orientation of the hexagonal lattice and the primitive lattice vectors $\mathbf{a}_1$, $\mathbf{a}_2$. b) The rotated BZ and Dirac points $\mathbf{K}^\theta$ of graphene, along with the wavenumbers $\mathbf{k}'_j$ in the BZ of the TMDC. As θ changes in the range $[0..\pi/3]$, the $\mathbf{k}'_j$ trace out the arcs shown by dashed lines. c) Reflection planes of the hexagonal BZ. $\mathcal{R}^{(1,2,3)}_v$ is relevant for both graphene and the TMDC, $\mathcal{R}^{(1,2,3)}_d$ only for graphene.

$(H_{\rm soc})_{bs,b's'}$ denote the matrix elements of the spin-orbit coupling operator $\hat{H}_{soc}$ between Bloch wavefunctions corresponding to bands b and b' of the monolayer TMDC. For our purposes the matrix elements between an even $\Psi^{(e)}_{tmdc}(\tau\mathbf{k}'_j,\mathbf{r})$ and an odd $\Psi^{(o)}_{tmdc}(\tau\mathbf{k}'_j,\mathbf{r})$ Bloch states are important and they can be written as

$$H_{e,o}(\tau\mathbf{k}'_j) = \langle\Psi^{(e)}_{tmdc}(\tau\mathbf{k}'_j,\mathbf{r})|\hat{H}_{soc}|\Psi^{(o)}_{tmdc}(\tau\mathbf{k}'_j,\mathbf{r})\rangle = i\lambda_{soc}\left[\alpha^{(x)}_{e,o}(\tau\mathbf{k}'_j)s_x + \alpha^{(y)}_{e,o}(\tau\mathbf{k}'_j)s_y\right]. \tag{4}$$

Here λ_{soc} characterizes the strength of the intrinsic SOC in the TMDC layer. $\hat{H}_{soc} \sim \hat{L}_x\hat{S}_x + \hat{L}_y\hat{S}_y + \hat{L}_z\hat{S}_z = \frac{1}{2}(\hat{L}_+\hat{S}_- + \hat{L}_-\hat{S}_+) + \hat{L}_z\hat{S}_z$, $\hat{L}_{x,y,z}$ are angular momentum operators, $\hat{L}_\pm = \hat{L}_x \pm i\hat{L}_y$, $\hat{S}_{x,y,z} = \frac{\hbar}{2}s_{x,y,z}$ are spin operators and the Pauli matrices $s_{x,y,z}$ act on the spin degree of freedom. The complex numbers $\alpha^{(x,y)}_{e,o}(\tau\mathbf{k}'_j)$ are defined as

$$i\,\alpha^{(x)}_{e,o}(\tau\mathbf{k}'_j) = \langle\Psi^{(e)}_{tmdc}(\tau\mathbf{k}'_j,\mathbf{r})\left|\hat{L}_x\right|\Psi^{(o)}_{tmdc}(\tau\mathbf{k}'_j,\mathbf{r})\rangle, \tag{5a}$$

$$i\,\alpha^{(x)}_{e,o}(\tau\mathbf{k}'_j) = \langle\Psi^{(e)}_{tmdc}(\tau\mathbf{k}'_j,\mathbf{r})\left|\hat{L}_y\right|\Psi^{(o)}_{tmdc}(\tau\mathbf{k}'_j,\mathbf{r})\rangle. \tag{5b}$$

One can make use of the fact that the $\tau\mathbf{k}'_j$ vectors are related by $2\pi/3$ rotations, which is also a symmetry of the TMDC lattice. Following Ref. [3] one may write $\Psi^{(e(o))}_{tmdc}(\mathcal{R}_{\pm2\pi/3}\tau\mathbf{k}'_j,\mathbf{r}) = \mathcal{R}_{\pm2\pi/3}\Psi^{(e(o))}_{tmdc}(\tau\mathbf{k}'_j,\mathbf{r})$ where $\mathcal{R}_{\pm2\pi/3}$ denotes rotation by $\pm2\pi/3$. Substituting this into Eq. (4) and taking into account that $\mathcal{R}_{2\pi/3}\hat{L}_\pm(\mathcal{R}_{2\pi/3})^\dagger = e^{\mp i2\pi/3}L_\pm$, one finds

$$H_{e,o}(\tau\mathbf{k}'_j) = i\lambda_{soc}\begin{pmatrix} 0 & \alpha^{(-)}_{e,o}(\tau\mathbf{k}'_1)e^{-i(j-1)2\pi/3} \\ \alpha^{(+)}_{e,o}(\tau\mathbf{k}'_1)e^{i(j-1)2\pi/3} & 0 \end{pmatrix}, \tag{6}$$

where $\alpha^{(\pm)}_{e,o}(\mathbf{k}'_1) = \alpha^{(x)}_{e,o}(\tau\mathbf{k}'_1) \pm i\alpha^{(y)}_{e,o}(\tau\mathbf{k}'_1)$.

B. Derivation of ϑ_R and λ_R

It is instructive to consider the contribution of a single pair of $b = e$ and $b' = o$ bands in Eq. (1). Using Eq.(2), one finds

$$(H_R^{gr})_{e,o} = \sum_j \begin{pmatrix} 1 & e^{i\tau(\phi_j^A - \phi_j^B)} \\ e^{-i\tau(\phi_j^A - \phi_j^B)} & 1 \end{pmatrix} \otimes \frac{\left[t_{e,o}(\tau\mathbf{k}'_j)H_{e,o}(\tau\mathbf{k}'_j) + t_{o,e}(\tau\mathbf{k}'_j)H_{o,e}(\tau\mathbf{k}'_j)\right]}{[E_D^{\rm gr} - E_e^{\rm tmdc}(\tau\mathbf{k}'_j)][E_D^{\rm gr} - E_o^{\rm tmdc}(\tau\mathbf{k}'_j)]}$$
$$= \sum_j \mathbf{M}_j(\tau\phi_j^A, \tau\phi_j^B) \otimes \frac{\left[t_{e,o}(\tau\mathbf{k}'_j)H_{e,o}(\tau\mathbf{k}'_j) + t_{o,e}(\tau\mathbf{k}'_j)H_{o,e}(\tau\mathbf{k}'_j)\right]}{[E_D^{\rm gr} - E_e^{\rm tmdc}(\tau\mathbf{k}'_j)][E_D^{\rm gr} - E_o^{\rm tmdc}(\tau\mathbf{k}'_j)]} \quad (7)$$

As explained in Sec. I A, the phases $\phi_j^{A,B}$ in $\mathbf{M}_j(\tau\phi_j^A, \tau\phi_j^B)$ are defined as $\phi_j^{A,B} = \boldsymbol{t}_{A,B} \cdot \mathbf{G}_j$. There are a number of possible choices for the vectors $\boldsymbol{t}_{A,B}$ and for the primitive reciprocal lattice vectors $\mathbf{b}_{1,2}$ of graphene, and the latter determine $\mathbf{G}_j$. For a given j the phase $\phi_j^{A,B}$ depends on these choices, but in general $\phi_j^{A,B} \in \{0, 2\pi/3, -2\pi/3\}$. The different choices lead to unitary equivalent $\mathbf{M}'_j(\tau\phi_j^A, \tau\phi_j^B) = \mathbf{U}(\tau)\mathbf{M}_j(\tau\phi_j^A, \tau\phi_j^B)\mathbf{U}^\dagger(\tau)$ matrices and hence unitary equivalent $(H_R^{gr})_{e,o}$ Hamiltonians. Importantly, $\mathbf{U}(\tau)$ does not depend on the geometric twist angle θ. Using Sec. I A 1, the $\mathbf{M}_j$ matrices read

$$\mathbf{M}_j(\tau\phi_j^A, \tau\phi_j^B) = \begin{pmatrix} 1 & e^{i\tau\frac{2\pi}{3}j} \\ e^{-i\tau\frac{2\pi}{3}j} & 1 \end{pmatrix}. \quad (8)$$

Furthermore, $H_{o,e}(\tau\mathbf{k}'_j) = [H_{e,o}(\tau\mathbf{k}'_j)]^\dagger$, $t_{e,o}(\tau\mathbf{k}'_j) = t_e(\tau\mathbf{k}'_j)t_o^*(\tau\mathbf{k}'_j) = (-1)^\mu |t_{e,o}(\tau\mathbf{k}'_j)|e^{i\eta(\tau\mathbf{k}'_j)}$ and $t_{o,e}(\tau\mathbf{k}'_j) = t_{e,o}^*(\tau\mathbf{k}'_j)$. We define $\eta(\tau\mathbf{k}'_j) = \mathrm{Arg}[t_{e,o}(\tau\mathbf{k}'_j)] \bmod \pi$ and, as it will be explained in more detail in Sec. I C, the index $\mu = 0, 1$ gives the sign of the induced Rashba SOC which depends on the layer stacking. Note that the phase factors $e^{i\tau\boldsymbol{G}_j^\theta \cdot \boldsymbol{d}_0}$, which encode the effect of a lateral shift between the layers in Eq. (2), have dropped out of the calculations. This means that our results for the induced Rashba SOC do not depend on such shift. The same conclusion holds for the valley Zeeman SOC as well, which depends on $|t_b(\tau\mathbf{k}'_j)|^2$, see Ref. 1.

Because of the C_3 symmetry of the system, $t_{e,o}(\tau\mathbf{k}'_j)$ does not depend on the index j and from time reversal symmetry follows that $t_{e,o}(-\mathbf{k}'_1) = t_{e,o}^*(\mathbf{k}'_1)$. Therefore, by taking into account Eq. (6),

$$t_{e,o}(\tau\mathbf{k}'_j)H_{e,o}(\tau\mathbf{k}'_j) + t_{e,o}^*(\tau\mathbf{k}'_j)[H_{e,o}(\tau\mathbf{k}'_j)]^\dagger = 2i\lambda_{soc}|t_{e,o}(\tau\mathbf{k}'_1)| \begin{pmatrix} 0 & \Lambda_{e,o}(\tau\mathbf{k}'_1)e^{-i(j-1)2\pi/3} \\ -\Lambda_{e,o}^*(\tau\mathbf{k}'_1)e^{i(j-1)2\pi/3} & 0 \end{pmatrix}, \quad (9)$$

where $\Lambda_{e,o}(\tau\mathbf{k}'_1) = Im[e^{i\eta(\tau\mathbf{k}'_1)}\alpha_{e,o}^{(y)}(\tau\mathbf{k}'_1)] + iIm[e^{i\eta(\tau\mathbf{k}'_1)}\alpha_{e,o}^{(x)}(\tau\mathbf{k}'_1)]$. One can show that $\Lambda_{e,o}(\tau\mathbf{k}'_1) = \tau\Lambda_{e,o}(\mathbf{k}'_1)$ and one may write $\Lambda_{e,o}(\mathbf{k}'_1) = |\Lambda_{e,o}(\mathbf{k}'_1)|e^{i\tilde{\vartheta}_{e,o}(\mathbf{k}'_1)}$, where

$$\tilde{\vartheta}_{e,o}(\mathbf{k}'_1) = \mathrm{Arg}[\Lambda_{e,o}(\mathbf{k}'_1)] = \mathrm{Arctan}\left[\frac{\mathrm{Im}[e^{i\eta(\mathbf{k}'_1)}\alpha_{e,o}^{(x)}(\mathbf{k}'_1)]}{\mathrm{Im}[e^{i\eta(\mathbf{k}'_1)}\alpha_{e,o}^{(y)}(\mathbf{k}'_1)]}\right] + m\pi, \qquad m = 0, \pm1, \pm2 \ldots \quad (10)$$

Here Im[...] denotes the imaginary part. $\tilde{\vartheta}_{e,o}(\mathbf{k}'_1)$ is a quantum phase which depends on i) the phase $\eta(\mathbf{k}'_1)$ of the interlayer tunneling amplitude between the Bloch states of graphene and the TMDC layer and ii) on off-diagonal matrix elements of the intrinsic SOC of the TMDC layer defined in Eq.(4).

Due to C_3 symmetry, the denominator of Eq. (7) is the same for all j and because of time reversal symmetry it does not depend on τ. Therefore the denominator can be pulled out of the summation. Substituting Eqs. (8) and (9) into Eq. (7) and performing the summation over j one finds

$$(H_R^{gr})_{e,o} = \lambda_{R,(e,o)}(\mathbf{k}'_1)e^{i\frac{s_z}{2}\vartheta_{e,o}(\mathbf{k}'_1)} \begin{pmatrix} 0 & 0 & 0 & i\frac{\tau+1}{2} \\ 0 & 0 & -i\frac{\tau-1}{2} & 0 \\ 0 & i\frac{\tau-1}{2} & 0 & 0 \\ -i\frac{\tau+1}{2} & 0 & 0 & 0 \end{pmatrix} e^{-i\frac{s_z}{2}\vartheta_{e,o}(\mathbf{k}'_1)}. \quad (11)$$

Here we defined

$$\vartheta_{e,o}(\mathbf{k}_1') = \tilde{\vartheta}_{e,o}(\mathbf{k}_1') + 2\pi/3, \tag{12}$$

and $\lambda_{R,(e,o)}(\mathbf{k}_1')$ is given by[1]

$$\lambda_{R,(e,o)}(\mathbf{k}_1') = \frac{(-1)^{\mu} 6\lambda_{soc} |t_{e,o}(\mathbf{k}_1')||\Lambda_{e,o}(\mathbf{k}_1')|}{[E_D^{\rm gr} - E_e^{\rm tmdc}(\mathbf{k}_1')]\,[E_D^{\rm gr} - E_o^{\rm tmdc}(\mathbf{k}_1')]}. \tag{13}$$

Using the τ_z Pauli matrix, one may rewrite Eq. (11) in a more compact form:

$$(H_R^{gr})_{e,o} = -\frac{\lambda_{R,(e,o)}(\mathbf{k}_1')}{2} e^{i\frac{s_z}{2}\vartheta_{e,o}(\mathbf{k}_1')} \left(\tau_z \sigma_x s_y + \sigma_y s_x\right) e^{-i\frac{s_z}{2}\vartheta_{e,o}(\mathbf{k}_1')}. \tag{14}$$

Note, that in the derivation of Eqs. (12)-(14) we only made use of time reversal symmetry and that the $\mathbf{k}_j'$ vectors are related by $2\pi/3$ rotations. Therefore these results are valid for arbitrary interlayer twist angle θ. On the other hand, we considered the contribution of a single pair of e and o bands of the TMDC to the induced Rashba type SOC. As Eq. (1) shows, one needs to sum over all q pairs of (e,o) bands and one may define the complex Rashba SOC coefficient by

$$\bar{\lambda}_R = \sum_q \lambda_{{\rm R},(e,o)_q} e^{i\vartheta_{(e,o)_q}}. \tag{15}$$

In terms of its magnitude $\lambda_R(\mathbf{k}_1') = |\bar{\lambda}_R(\mathbf{k}_1')|$ and phase $\vartheta_R(\mathbf{k}_1') = {\rm Arg}[\bar{\lambda}_R(\mathbf{k}_1')]$, the Hamiltonian of the induced Rashba SOC can be written as

$$H_R^{gr} = -\frac{\lambda_R(\mathbf{k}_1')}{2} e^{i\frac{s_z}{2}\vartheta_R(\mathbf{k}_1')} \left(\tau_z \sigma_x s_y + \sigma_y s_x\right) e^{-i\frac{s_z}{2}\vartheta_R(\mathbf{k}_1')}. \tag{16}$$

Note, that both $\lambda_R(\mathbf{k}_1')$ and $\vartheta_R(\mathbf{k}_1')$ depend implicitly on θ through $\mathbf{k}_1'$, as shown in Fig. 1. We will discuss the θ dependence of ϑ_R in more detail in Sec. I E.

C. Staking order dependent sign of λ_R

In our theory the sign of λ_R depends on the stacking order of the graphene and the TMDC layers, i.e., whether is graphene below or above the TMDC layer. Such a sign has no physical significance in TMDC/graphene bilayer stacks, but it is important in TMDC/graphene/TMDC trilayers, because it means that the contributions of the two TMDC layers to the induced Rashba SOC add up with an opposite sign.

As explained below Eq. (8), the induced Rashba SOC is a second order process in interlayer tunneling. The tunneling amplitude is given by $t_{e,o}(\tau\mathbf{k}_j') = t_e(\tau\mathbf{k}_j')t_o^*(\tau\mathbf{k}_j')$, i.e., it depends on the product of the tunneling amplitudes to an e and to an o band of the TMDC. $\Psi_{tmdc}^{(e)}(\mathbf{r})$ of an e band of the TMDC is even with respect to the mirror plane that contains the metal atoms of the TMDC layer. However, the graphene p_z orbitals have a different sign above and below the graphene layer. Therefore one can expect that the matrix element given in Eq. (2) between the graphene Bloch wavefunction $\Psi_{gr}(\mathbf{r})$ and $\Psi_{tmdc}^{(e)}(\mathbf{r})$ should have a global sign difference depending on the stacking order of the two layers, i.e., whether the graphene layer is above or below the TMDC layer. On the other hand, similar consideration suggests that the sign of the amplitude $t_o(\tau\mathbf{k}_j')$ between $\Psi_{gr}(\mathbf{r})$ and $\Psi_{tmdc}^{(o)}(\mathbf{r})$ does not depend on the stacking order. Therefore, there will be a stacking order dependent sign factor in $t_{e,o}(\tau\mathbf{k}_j') = t_e(\tau\mathbf{k}_j')t_o^*(\tau\mathbf{k}_j')$, which is described by the index $\mu = 0, 1$ introduced below Eq. (8). The stacking order dependence of $t_e(\tau\mathbf{k}_j')$ and $t_o(\tau\mathbf{k}_j')$ can be explicitly shown if they are calculated e.g., using the two-center Slater-Koster parametrization of the corresponding transfer integrals, see Refs.[1, 4] for details.

Because of this stacking order dependent sign, the induced Rashba type SOC in TMDC/graphene/TMDC trilayers, which is given by the sum of the contributions from the two TMDC layer, reads $H_R^{(tls)} = H_R^{(b)} - H_R^{(t)}$. Taking into account the interlayer twist angle dependence of λ_R (see Sec. II C) and of $\theta + \vartheta_R$ (shown in Fig.1 of the main text) one can then easily see that $H_R^{(tls)}$ vanishes whenever the TMDC/graphene/TMDC stack is either inversion symmetric or has a horizontal mirror symmetry.

D. Effects of the interlayer twist

H_R^{gr} in Eq. (16) was obtained in the $x'-y'$ coordinate system of the TMDC layer (see Fig. 2), where the matrix elements of $\hat{H}_{soc}$ were evaluated. Our choice of reciprocal lattice vectors leads to $H_{orb}^{gr} = v_F(\tau_z\sigma_x\delta k_x - \sigma_y\delta k_y)$ for the orbital Hamiltonian of graphene in the $x-y$ coordinate system, where $\delta\mathbf{k} = (\delta k_x, \delta k_y)$ is a small wavevector measured from the $\tau\mathbf{K}$ point. In the $x'-y'$ system H_{orb}^{gr} is given by $H_{orb}^{gr,\theta} = e^{-i\tau_z\frac{\sigma_z}{2}\theta}H_{orb}^{gr}e^{i\tau_z\frac{\sigma_z}{2}\theta}$. The total effective Hamiltonian of graphene is therefore

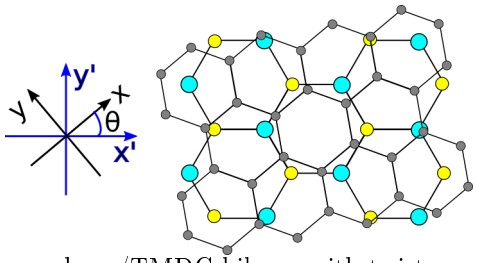

FIG. 2: Schematics of a twisted graphene/TMDC bilayer with twist angle θ and the coordinate systems $x-y$ and $x'-y'$.

$$H_{\rm eff}^{gr,\theta} = e^{-i\tau_z\frac{\sigma_z}{2}\theta}H_{orb}^{gr}e^{i\tau_z\frac{\sigma_z}{2}\theta} + H_R^{gr} + H_{vZ}^{gr}, \tag{17}$$

where we have also taken into account the valley-Zeeman induced SOC, which is described by

$$H_{vZ}^{gr} = \lambda_{vZ}\tau_z s_z. \tag{18}$$

H_{vZ}^{gr} is invariant under rotations around the $\hat{z}$ axis and has the same form in both the $x-y$ and $x'-y'$ coordinate systems. One may perform a unitary transformation $e^{i\tau_z\frac{\sigma_z}{2}\theta}H_{\rm eff}^{gr,\theta}e^{-i\tau_z\frac{\sigma_z}{2}\theta}$. This transformation leaves H_{vZ} unchanged and one finds

$$H_{\rm eff}^{gr} = H_{orb}^{gr} + e^{i\tau_z\frac{\sigma_z}{2}\theta}H_R^{gr}e^{-i\tau_z\frac{\sigma_z}{2}\theta} + H_{vZ}^{gr}. \tag{19}$$

It is convenient to perform another unitary transformation $H_{\rm eff}^{gr} \to \sigma_x H_{\rm eff}^{gr}\sigma_x$. This changes the orbital Hamiltonian $v_F(\tau_z\sigma_x\delta k_x - \sigma_y\delta k_y) \to v_F(\tau_z\sigma_x\delta k_x + \sigma_y\delta k_y)$, leaves H_{vZ}^{gr} unchanged, and transforms the Rashba Hamiltonian to

$$\sigma_x e^{i\tau_z\frac{\sigma_z}{2}\theta}H_R^{gr}e^{-i\tau_z\frac{\sigma_z}{2}\theta}\sigma_x = -\frac{\lambda_R(\mathbf{k}_1')}{2}e^{-i\tau_z\frac{\sigma_z}{2}\theta}e^{i\frac{s_z}{2}\vartheta_R(\mathbf{k}_1')}\left(\tau_z\sigma_x s_y - \sigma_y s_x\right)e^{-i\frac{s_z}{2}\vartheta_R(\mathbf{k}_1')}e^{i\tau_z\frac{\sigma_z}{2}\theta}. \tag{20}$$

Eq. (20) shows more explicitly the effects of interlayer rotation on the graphene Rashba Hamiltonian $\tilde{H}_R^{gr} = \frac{\lambda_R}{2}\left(\tau_z\sigma_x s_y - \sigma_y s_x\right)$ derived previously in Refs. [5, 6]: i) $\tilde{H}_R^{gr}$ is rotated in real space by θ, an ii) if $\vartheta_R \neq 2m\pi$, m integer, then a rotation in spin-space appears.

E. Calculation of ϑ_R for $\theta = 0$, $\theta = \pi/6$ and $\theta = \pi/3$ twist angles

The calculations of Sec. I B are valid for arbitrary interlayer twist angle θ. For $\theta_l = l\pi/6$, $l = 0, 1, 2\ldots$ the graphene/TMDC bilayer has a higher, C_{3v} symmetry, which implies further constraints on the form of H_R^{gr}. By calculating $\vartheta_{e,o}(\mathbf{k}_1')$ defined in Eq. (12) for $\theta = 0, \pi/6, \pi/3$ explicitly, we show how the results of Sec. I B are simplified in this case.

1. $\theta = 0$ *twist angle*

In Fig. 3 we show the wavevectors $\mathbf{k}_{1,2,3}'$ that satisfy the quasimomentum conservation as well as the three reflection planes $\mathcal{R}_v^{(1,2,3)}$ that the system possess in addition to the C_3 symmetry. First, we will derive a useful relation for the tunneling amplitude $t_{e,o}(\mathbf{k}_1') = t_e(\mathbf{k}_1')t_o^*(\mathbf{k}_1')$, defined below Eq. (8).

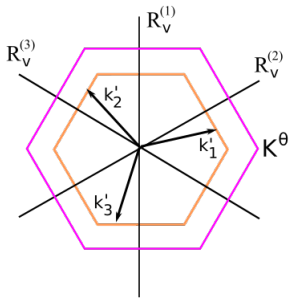

FIG. 3: The BZ of graphene (purple) and of the TMDC (orange), along with $\mathbf{k}'_{1,2,3}$ vectors and the reflection planes $\mathcal{R}_v^{1,2,3}$ for $\theta = 0$.

Using the definition $t_{e(o)}(\tau\mathbf{k}'_j)$ given in Eq.(2) and denoting $\mathbf{K}^{\theta=0} = \mathbf{K}^{(0)}$, consider the following:

$$
\begin{aligned}
t_{e(o)}(\mathbf{k}'_1)e^{-i\phi_1^X} &= \langle\Psi_{gr}^{(X)}(\mathbf{K}_1^{(0)},\mathbf{r})|H_{orb}|\Psi_{tmdc}^{(e(o))}(\mathbf{k}'_1,\mathbf{r})\rangle = \langle(H_{orb}\Psi_{tmdc}^{(e(o))}(\mathbf{k}'_1,\mathbf{r}))^*|(\Psi_{gr}^{(X)}(\mathbf{K}_1^{(0)},\mathbf{r}))^*\rangle \\
&= \langle H_{orb}(\Psi_{tmdc}^{(e(o))}(\mathbf{k}'_1,\mathbf{r}))^*|(\Psi_{gr}^{(X)}(\mathbf{K}_1^{(0)},\mathbf{r}))^*\rangle = \langle H_{orb}\Psi_{tmdc}^{(e(o))}(-\mathbf{k}'_1,\mathbf{r})|\Psi_{gr}^{(X)}(-\mathbf{K}_1^{(0)},\mathbf{r})\rangle \\
&= \langle H_{orb}\Psi_{tmdc}^{(e(o))}(\mathcal{R}_v^{(2)}(\mathbf{k}'_1-\mathbf{b}'_1),\mathbf{r})|\Psi_{gr}^{(X)}(\mathcal{R}_v^{(1)}\mathbf{K}_1^{(0)},\mathbf{r})\rangle \\
&= \langle H_{orb}\mathcal{R}_v^{(2)}\Psi_{tmdc}^{(e(o))}(\mathbf{k}'_1-\mathbf{b}'_1,\mathbf{r})|\Psi_{gr}^{(X)}(\mathcal{R}_v^{(1)}\mathbf{K}_1^{(0)},\mathbf{r})\rangle \\
&= \langle \mathcal{R}_v^{(2)}H_{orb}\Psi_{tmdc}^{(e(o))}(\mathbf{k}'_1-\mathbf{b}'_1,\mathbf{r})|\Psi_{gr}^{(X)}(\mathcal{R}_v^{(1)}\mathbf{K}_1^{(0)},\mathbf{r})\rangle \\
&= \langle H_{orb}\Psi_{tmdc}^{(e(o))}(\mathbf{k}'_1-\mathbf{b}'_1,\mathbf{r})|\mathcal{R}_v^{(2)}\Psi_{gr}^{(X)}(\mathcal{R}_v^{(1)}\mathbf{K}_1^{(0)},\mathbf{r})\rangle \\
&= \langle H_{orb}\Psi_{tmdc}^{(e(o))}(\mathbf{k}'_1-\mathbf{b}'_1,\mathbf{r})|\Psi_{gr}^{(X)}(\mathcal{R}_v^{(2)}\mathcal{R}_v^{(1)}\mathbf{K}_1^{(0)},\mathbf{r})\rangle \\
&= \langle H_{orb}\Psi_{tmdc}^{(e(o))}(\mathbf{k}'_1-\mathbf{b}'_1,\mathbf{r})|\Psi_{gr}^{(X)}(\mathbf{K}_1^{(0)}-\mathbf{b}_1^{(0)},\mathbf{r})\rangle \\
&= \left(\langle\Psi_{gr}^{(X)}(\mathbf{K}_1^{(0)}-\mathbf{b}_1^{(0)},\mathbf{r})|H_{orb}|\Psi_{tmdc}^{(e(o))}(\mathbf{k}'_1-\mathbf{b}'_1,\mathbf{r})\rangle\right)^* \\
&= \left(e^{-i\omega_1^X}\langle\Psi_{gr}^{(X)}(\mathbf{K}_1^{(0)},\mathbf{r})|H_{orb}|\Psi_{tmdc}^{(e(o))}(\mathbf{k}'_1,\mathbf{r})\rangle e^{i\omega_1^{(e(o))}}\right)^* = t_{e(o)}^*(\mathbf{k}'_1)e^{i\phi_1^X}e^{i\omega_1^X}e^{-i\omega_1^{(e(o))}}.
\end{aligned}
\tag{21}
$$

Here we have made use of i) time reversal symmetry when assuming $H_{orb}^* = H_{orb}$, ii) $\mathcal{R}_v^{(2)} = (\mathcal{R}_v^{(2)})^{-1}$, and iii) $\mathcal{R}_v^{(2)}$ is a symmetry of the system therefore $\mathcal{R}_v^{(2)}H_{orb} = H_{orb}\mathcal{R}_v^{(2)}$. Moreover, Bloch wavefunctions at equivalent wavenumbers can differ at most by a phase factor, i.e., $|\Psi_{gr}^{(X)}(\mathbf{K}_1^{(0)}-\mathbf{b}_1^{(0)},\mathbf{r})\rangle = |\Psi_{gr}^{(X)}(\mathbf{K}_1^{(0)},\mathbf{r})\rangle e^{i\omega_1^X}$ and $|\Psi_{tmdc}^{(e(o))}(\mathbf{k}'_1-\mathbf{b}'_1,\mathbf{r})\rangle = |\Psi_{tmdc}^{(e(o))}(\mathbf{k}'_1,\mathbf{r})\rangle e^{i\omega_1^{(e(o))}}$. From Eq. (21) one finds that

$$
t_{e,o}(\mathbf{k}'_1) = t_e(\mathbf{k}'_1)t_o^*(\mathbf{k}'_1) = t_{e,o}^*(\mathbf{k}'_1)e^{-i\omega_1^{(e)}}e^{i\omega_1^{(o)}}. \tag{22}
$$

A similar relation can be derived for the matrix elements of $\hat{H}_{soc}$, namely, for $\langle\Psi^{(e)}(\mathbf{k}'_1,\mathbf{r})|L_\pm|\Psi^{(o)}(\mathbf{k}'_1,\mathbf{r})\rangle$:

$$
\begin{aligned}
\langle\Psi^{(e)}(\mathbf{k}'_1,\mathbf{r})|L_\pm|\Psi^{(o)}(\mathbf{k}'_1,\mathbf{r})\rangle &= \langle(L_\pm\Psi^{(o)}(\mathbf{k}'_1,\mathbf{r}))^*|(\Psi^{(e)}(\mathbf{k}'_1,\mathbf{r}))^*\rangle = -\langle L_\mp\Psi^{(o)}(-\mathbf{k}'_1,\mathbf{r})|\Psi^{(e)}(-\mathbf{k}'_1,\mathbf{r})\rangle \\
&= -\langle L_\mp\Psi^{(o)}(\mathcal{R}_v^{(2)}(\mathbf{k}'_1-\mathbf{b}'_1),\mathbf{r})|\Psi^{(e)}(\mathcal{R}_v^{(2)}(\mathbf{k}'_1-\mathbf{b}'_1),\mathbf{r})\rangle \\
&= -\langle L_\mp\mathcal{R}_v^{(2)}\Psi^{(o)}(\mathbf{k}'_1-\mathbf{b}'_1,\mathbf{r})|\mathcal{R}_v^{(2)}\Psi^{(e)}(\mathbf{k}'_1-\mathbf{b}'_1,\mathbf{r})\rangle \\
&= -\langle e^{\pm i\frac{2\pi}{3}}\mathcal{R}_v^{(2)}[L_\pm\Psi^{(o)}(\mathbf{k}'_1-\mathbf{b}'_1,\mathbf{r})]|\mathcal{R}_v^{(2)}\Psi^{(e)}(\mathbf{k}'_1-\mathbf{b}'_1,\mathbf{r})\rangle \\
&= -e^{\mp i\frac{2\pi}{3}}\langle[L_\pm\Psi^{(o)}(\mathbf{k}'_1-\mathbf{b}'_1,\mathbf{r})]|\Psi^{(e)}(\mathbf{k}'_1-\mathbf{b}'_1,\mathbf{r})\rangle \\
&= -e^{\mp i\frac{2\pi}{3}}\left(\langle\Psi^{(e)}(\mathbf{k}'_1-\mathbf{b}'_1,\mathbf{r})|L_\pm|\Psi^{(o)}(\mathbf{k}'_1-\mathbf{b}'_1,\mathbf{r})\rangle\right)^* \\
&= -e^{\mp i\frac{2\pi}{3}}\left(\langle\Psi^{(e)}(\mathbf{k}'_1,\mathbf{r})|L_\pm|\Psi^{(o)}(\mathbf{k}'_1,\mathbf{r})\rangle\right)^* e^{i\omega_1^{(e)}}e^{-i\omega_1^{(o)}}.
\end{aligned}
\tag{23}
$$

In terms of $\alpha^{(\pm)}_{e,o}(\mathbf{k}'_1)$, introduced after Eq. (6), Eq. (23) means that $\alpha^{(\pm)}_{e,o}(\mathbf{k}'_1) = -e^{\mp i\frac{2\pi}{3}}[\alpha^{(\pm)}_{e,o}(\mathbf{k}'_1)]^* e^{i\omega_1^{(e)}} e^{-i\omega_1^{(o)}}$. Therefore,

$$\begin{aligned}\alpha^{(x)}_{e,o}(\mathbf{k}_1) &= \frac{1}{2}\left(\alpha^{(+)}_{e,o}(\mathbf{k}'_1) + \alpha^{(-)}_{e,o}(\mathbf{k}'_1)\right) = -\frac{1}{2}\left(e^{-i\frac{2\pi}{3}}[\alpha^{(+)}_{e,o}(\mathbf{k}'_1)]^* + e^{i\frac{2\pi}{3}}[\alpha^{(-)}_{e,o}(\mathbf{k}'_1)]^*\right) e^{i\omega_1^{(e)}} e^{-i\omega_1^{(o)}} \\ &= -\frac{1}{2}\left(-\frac{1}{2}\left([\alpha^{(+)}_{e,o}(\mathbf{k}'_1)]^* + [\alpha^{(-)}_{e,o}(\mathbf{k}'_1)]^*\right) - i\frac{\sqrt{3}}{2}\left([\alpha^{(+)}_{e,o}(\mathbf{k}'_1)]^* - [\alpha^{(-)}_{e,o}(\mathbf{k}'_1)]^*\right)\right) e^{i\omega_1^{(e)}} e^{-i\omega_1^{(o)}}, \quad (24a)\end{aligned}$$

$$\begin{aligned}\alpha^{(y)}_{e,o}(\mathbf{k}_1) &= \frac{1}{2i}\left(\alpha^{(+)}_{e,o}(\mathbf{k}'_1) - \alpha^{(-)}_{e,o}(\mathbf{k}'_1)\right) = -\frac{1}{2i}\left(e^{-i\frac{2\pi}{3}}[\alpha^{(+)}_{e,o}(\mathbf{k}'_1)]^* - e^{i\frac{2\pi}{3}}[\alpha^{(-)}_{e,o}(\mathbf{k}'_1)]^*\right) e^{i\omega_1^{(e)}} e^{-i\omega_1^{(o)}} \\ &= -\frac{1}{2i}\left(-\frac{1}{2}\left([\alpha^{(+)}_{e,o}(\mathbf{k}'_1)]^* - [\alpha^{(-)}_{e,o}(\mathbf{k}'_1)]^*\right) - i\frac{\sqrt{3}}{2}\left([\alpha^{(+)}_{e,o}(\mathbf{k}'_1)]^* + [\alpha^{(-)}_{e,o}(\mathbf{k}'_1)]^*\right)\right) e^{i\omega_1^{(e)}} e^{-i\omega_1^{(o)}}. \quad (24b)\end{aligned}$$

Eqs. (24) can be written as

$$\begin{pmatrix}\alpha^{(x)}_{e,o}(\mathbf{k}'_1)\\ \alpha^{(y)}_{e,o}(\mathbf{k}'_1)\end{pmatrix} = -\frac{1}{2}\begin{pmatrix}1 & \sqrt{3}\\ \sqrt{3} & -1\end{pmatrix}\begin{pmatrix}\left(\alpha^{(x)}_{e,o}(\mathbf{k}'_1)\right)^*\\ \left(\alpha^{(y)}_{e,o}(\mathbf{k}'_1)\right)^*\end{pmatrix} e^{i\omega_1^{(e)}} e^{-i\omega_1^{(o)}}, \quad (25)$$

One now calculate $\vartheta_{e,o}(\mathbf{k}'_1)$ for $\theta = 0$. First, combining Eq. (22) and Eq. (25) one arrives at

$$t_{e,o}(\mathbf{k}'_1)\begin{pmatrix}\alpha^{(x)}_{e,o}(\mathbf{k}'_1)\\ \alpha^{(y)}_{e,o}(\mathbf{k}'_1)\end{pmatrix} = -\frac{1}{2}\begin{pmatrix}1 & \sqrt{3}\\ \sqrt{3} & -1\end{pmatrix}\begin{pmatrix}\left(\alpha^{(x)}_{e,o}(\mathbf{k}'_1)\right)^*\\ \left(\alpha^{(y)}_{e,o}(\mathbf{k}'_1)\right)^*\end{pmatrix} t^*_{e,o}(\mathbf{k}'_1). \quad (26)$$

This means that $\mathrm{Im}\left[t_{e,o}(\mathbf{k}'_1)\alpha^{(x)}_{e,o}(\mathbf{k}'_1)\right] = -\frac{1}{2}\mathrm{Im}\left[[t_{e,o}(\mathbf{k}'_1)\alpha^{(x)}_{e,o}(\mathbf{k}'_1)]^*\right] - \frac{\sqrt{3}}{2}\mathrm{Im}\left[[t_{e,o}(\mathbf{k}'_1)\alpha^{(y)}_{e,o}(\mathbf{k}'_1)]^*\right]$, i.e., $\mathrm{Im}\left[t_{e,o}(\mathbf{k}'_1)\alpha^{(x)}_{e,o}(\mathbf{k}'_1)\right] = \sqrt{3}\,\mathrm{Im}\left[t_{e,o}(\mathbf{k}'_1)\alpha^{(y)}_{e,o}(\mathbf{k}'_1)\right]$. Regarding Eq. (10), it follows that

$$\mathrm{Arctan}\left[\frac{\mathrm{Im}[e^{i\eta(\mathbf{k}'_1)}\alpha^{(x)}_{e,o}(\mathbf{k}'_1)]}{\mathrm{Im}[e^{i\eta(\mathbf{k}'_1)}\alpha^{(y)}_{e,o}(\mathbf{k}'_1)]}\right] = \mathrm{Arctan}\left[\frac{\mathrm{Im}[t_{e,o}(\mathbf{k}'_1)\alpha^{(x)}_{e,o}(\mathbf{k}'_1)]}{\mathrm{Im}[t_{e,o}(\mathbf{k}'_1)\alpha^{(y)}_{e,o}(\mathbf{k}'_1)]}\right] = \frac{\pi}{3}, \quad (27)$$

and using Eq. (12) one finds $\vartheta_{e,o}(\mathbf{k}'_1) = (m+1)\pi$. Therefore, one finds from Eq. (20) that for $\theta = 0$ $H^{gr}_R = (-1)^m \frac{\lambda_R(\mathbf{k}'_1)}{2}\left(\tau_z\sigma_x s_y - \sigma_y s_x\right)$.

2. $\theta = \pi/6$ *twist angle*

Graphene has two, inequivalent sets of vertical reflection planes, see Fig. 1. For $\theta = \pi/6$, the $\mathcal{R}_d^{(1,2,3)}$ set aligns with the TMDC's $\mathcal{R}_v^{(1,2,3)}$ reflection planes, therefore the stack again has C_{3v} symmetry.

We denote the three wavevectors in the BZ of the TMDC that satisfy the quasimomentum conservation by $\tilde{\mathbf{k}}'_{1,2,3}$, see Fig. 4. As one can see, the $\tilde{\mathbf{k}}'_j$ vectors now lie on the Γ-M lines of the BZ of the TMDC. Let us consider the matrix element $\langle\Psi^{(e)}(\tilde{\mathbf{k}}_1,\mathbf{r})|L_\pm|\Psi^{(o)}(\tilde{\mathbf{k}}_1,\mathbf{r})\rangle$.

$$\begin{aligned}\langle\Psi^{(e)}(\tilde{\mathbf{k}}'_1,\mathbf{r})|L_\pm|\Psi^{(o)}(\tilde{\mathbf{k}}'_1,\mathbf{r})\rangle &= \langle\Psi^{(e)}(\tilde{\mathbf{k}}'_1,\mathbf{r})|(\mathcal{R}_v^{(3)})^\dagger\mathcal{R}_v^{(3)}L_\pm(\mathcal{R}_v^{(3)})^\dagger\mathcal{R}_v^{(3)}|\Psi^{(o)}(\tilde{\mathbf{k}}'_1,\mathbf{r})\rangle \\ &= \langle\Psi^{(e)}(\mathcal{R}_v^{(3)}\tilde{\mathbf{k}}'_1,\mathbf{r})|\mathcal{R}_v^{(3)}L_\pm(\mathcal{R}_v^{(3)})^\dagger|\Psi^{(o)}(\mathcal{R}_v^{(3)}\tilde{\mathbf{k}}'_1,\mathbf{r})\rangle \\ &= \langle\Psi^{(e)}(\tilde{\mathbf{k}}'_1,\mathbf{r})|\mathcal{R}_v^{(3)}L_\pm(\mathcal{R}_v^{(3)})^\dagger|\Psi^{(o)}(\tilde{\mathbf{k}}'_1,\mathbf{r})\rangle \\ &= e^{\pm i\frac{2\pi}{3}}\langle\Psi^{(e)}(\tilde{\mathbf{k}}'_1,\mathbf{r})|L_\mp|\Psi^{(o)}(\tilde{\mathbf{k}}'_1,\mathbf{r})\rangle, \quad (28)\end{aligned}$$

where we made use of $\mathcal{R}_v^{(3)}L_\pm(\mathcal{R}_v^{(3)})^\dagger = e^{\pm i\frac{2\pi}{3}}L_\mp$ and that $\mathcal{R}_v^{(3)}\tilde{\mathbf{k}}'_1 = \tilde{\mathbf{k}}'_1$. In terms of $\alpha^{(\pm)}_{e,o}(\mathbf{k}'_1)$, Eq.(28) can be rewritten as $\alpha^{(-)}_{e,o}(\tilde{\mathbf{k}}'_1) = e^{-i\frac{2\pi}{3}}\alpha^{(+)}_{e,o}(\tilde{\mathbf{k}}'_1)$. Therefore,

$$\alpha^{(x)}_{e,o}(\tilde{\mathbf{k}}'_1) = \frac{1}{2}\left(\alpha^{(+)}_{e,o}(\tilde{\mathbf{k}}'_1) + \alpha^{(-)}_{e,o}(\tilde{\mathbf{k}}'_1)\right) = \frac{1}{2}\left(1 + e^{-i\frac{2\pi}{3}}\right)\alpha^{(+)}_{e,o}(\tilde{\mathbf{k}}'_1), \quad (29a)$$

$$\alpha^{(y)}_{e,o}(\tilde{\mathbf{k}}'_1) = \frac{1}{2i}\left(\alpha^{(+)}_{e,o}(\tilde{\mathbf{k}}'_1) - \alpha^{(-)}_{e,o}(\tilde{\mathbf{k}}'_1)\right) = \frac{1}{2i}\left(1 - e^{-i\frac{2\pi}{3}}\right)\alpha^{(+)}_{e,o}(\tilde{\mathbf{k}}'_1). \quad (29b)$$

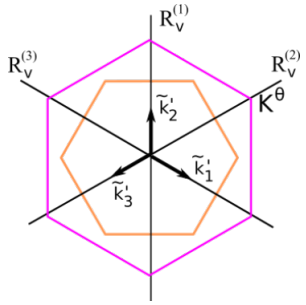

FIG. 4: The BZ of graphene (purple) and of the TMDC (orange), along with $\tilde{\mathbf{k}}'_{1,2,3}$ vectors and the reflection planes $\mathcal{R}_v^{1,2,3}$ for $\theta = \pi/6$.

It follows that $\alpha^{(y)}_{e,o}(\tilde{\mathbf{k}}'_1) = \sqrt{3}\alpha^{(x)}_{e,o}(\tilde{\mathbf{k}}'_1)$. Regarding Eq. (10), one finds $\text{Arctan}\left[\frac{\text{Im}[e^{i\eta(\tilde{\mathbf{k}}'_1)}\alpha^{(x)}_{e,o}(\tilde{\mathbf{k}}'_1)]}{\text{Im}[e^{i\eta(\tilde{\mathbf{k}}'_1)}\alpha^{(y)}_{e,o}(\tilde{\mathbf{k}}'_1)]}\right] = \frac{\pi}{6}$, and from Eq. (12) $\vartheta_{e,o}(\tilde{\mathbf{k}}'_1) = \frac{5\pi}{6} + m'\pi = (m'+1)\pi - \pi/6$.

3. $\theta = \pi/3$ twist angle

We again denote the three wavevectors in the BZ of the TMDC that satisfy the quasimomentum conservation by $\tilde{\mathbf{k}}'_{1,2,3}$, see Fig. 5. Note, that $\tilde{\mathbf{k}}'_1$ is related to $\mathbf{k}'_1$ in the $\theta = 0$ case by $\tilde{\mathbf{k}}'_1 = \mathcal{R}_v^{(3)}\mathbf{k}'_1$ and the $\mathbf{K}^{(\pi/3)}$ point of graphene is given by $-\mathbf{K}^{(0)} + \mathbf{b}^0_1$. This can be used to calculate the amplitude $t_{e(o)}(\tilde{\mathbf{k}}'_1)$ and

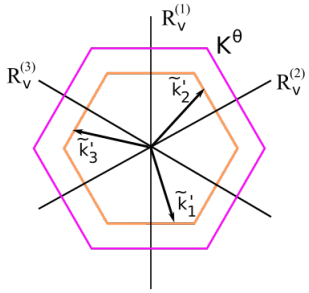

FIG. 5: The BZ of graphene (purple) and of the TMDC (orange), along with $\tilde{\mathbf{k}}'_{1,2,3}$ vectors and the reflection planes $\mathcal{R}_v^{1,2,3}$ for $\theta = \pi/3$.

$\alpha^{(\pm)}_{e,o}(\tilde{\mathbf{k}}'_1)$. Similarly to Eq. (21), one may write

$$\begin{aligned}
t_{e(o)}(\tilde{\mathbf{k}}'_1)e^{-i\phi_1^X} &= \langle\Psi^{(X)}_{gr}(\mathbf{K}_1^{(\pi/3)},\mathbf{r})|H_{orb}|\Psi^{(e(o))}_{tmdc}(\tilde{\mathbf{k}}'_1,\mathbf{r})\rangle \\
&= \langle\Psi^{(X)}_{gr}(-\mathbf{K}_1^{(0)}+\mathbf{b}_1^{(0)},\mathbf{r})|H_{orb}|\Psi^{(e(o))}_{tmdc}(\mathcal{R}_v^{(3)}\mathbf{k}'_1,\mathbf{r})\rangle \\
&= \langle\Psi^{(X)}_{gr}(-\mathbf{K}_1^{(0)}+\mathbf{b}_1^{(0)},\mathbf{r})|H_{orb}|\Psi^{(e(o))}_{tmdc}(\mathcal{R}_v^{(3)}\mathbf{k}'_1,\mathbf{r})\rangle \\
&= \langle\Psi^{(X)}_{gr}(-\mathbf{K}_1^{(0)}+\mathbf{b}_1^{(0)},\mathbf{r})|H_{orb}|\mathcal{R}_v^{(3)}\Psi^{(e(o))}_{tmdc}(\mathbf{k}'_1,\mathbf{r})\rangle \\
&= \langle\Psi^{(X)}_{gr}(-\mathbf{K}_1^{(0)}+\mathbf{b}_1^{(0)},\mathbf{r})|\mathcal{R}_v^{(3)}H_{orb}|\Psi^{(e(o))}_{tmdc}(\mathbf{k}'_1,\mathbf{r})\rangle \\
&= \langle\Psi^{(X)}_{gr}(\mathcal{R}_v^{(3)}(-\mathbf{K}_1^{(0)}+\mathbf{b}_1^{(0)}),\mathbf{r})|H_{orb}|\Psi^{(e(o))}_{tmdc}(\mathbf{k}'_1,\mathbf{r})\rangle \\
&= \langle\Psi^{(X)}_{gr}(\mathbf{K}_1^{(0)}-\mathbf{b}_1^{(0)}),\mathbf{r})|H_{orb}|\Psi^{(e(o))}_{tmdc}(\mathbf{k}'_1,\mathbf{r})\rangle = t_{e(o)}(\mathbf{k}'_1)e^{-i\phi_1^X}e^{-i\omega_1^X}.
\end{aligned} \tag{30}$$

This meas that $t_{e,o}(\tilde{\mathbf{k}}_1') = t_e(\tilde{\mathbf{k}}_1')t_o^*(\tilde{\mathbf{k}}_1') = t_e(\mathbf{k}_1')t_o^*(\mathbf{k}_1') = t_{e,o}(\mathbf{k}_1')$. Regarding the matrix elements of $\hat{H}_{soc}$, one finds

$$\begin{aligned}\langle\Psi^{(e)}(\tilde{\mathbf{k}}_1',\mathbf{r})|L_\pm|\Psi^{(o)}(\tilde{\mathbf{k}}_1',\mathbf{r})\rangle &= \langle\Psi^{(e)}(\mathcal{R}_v^{(3)}\mathbf{k}_1',\mathbf{r})|L_\pm|\Psi^{(o)}(\mathcal{R}_v^{(3)}\mathbf{k}_1',\mathbf{r})\rangle \\ &= \langle\Psi^{(e)}(\mathbf{k}_1',\mathbf{r})|[\mathcal{R}_v^{(3)}]^\dagger L_\pm\mathcal{R}_v^{(3)}|\Psi^{(o)}(\mathbf{k}_1',\mathbf{r})\rangle \\ &= e^{\pm i\frac{2\pi}{3}}\langle\Psi^{(e)}(\mathbf{k}_1',\mathbf{r})|L_\mp|\Psi^{(o)}(\mathbf{k}_1',\mathbf{r})\rangle\rangle \end{aligned} \tag{31}$$

Here we have used $[\mathcal{R}_v^{(3)}]^\dagger L_\pm\mathcal{R}_v^{(3)} = e^{\pm i\frac{2\pi}{3}}L_\mp$. Performing analogous calculations as in Eqs. (24), one finds

$$t_{e,o}(\tilde{\mathbf{k}}_1')\begin{pmatrix}\alpha_{e,o}^{(x)}(\tilde{\mathbf{k}}_1')\\ \alpha_{e,o}^{(y)}(\tilde{\mathbf{k}}_1')\end{pmatrix} = \frac{1}{2}\begin{pmatrix}-1 & \sqrt{3}\\ \sqrt{3} & 1\end{pmatrix}\begin{pmatrix}\alpha_{e,o}^{(x)}(\mathbf{k}_1')\\ \alpha_{e,o}^{(y)}(\mathbf{k}_1')\end{pmatrix}t_{e,o}(\mathbf{k}_1'). \tag{32}$$

One can now easily calculate $\vartheta_{e,o}(\tilde{\mathbf{k}}_1')$. Using Eq.(32)

$$\mathrm{Im}[t_{e,o}(\tilde{\mathbf{k}}_1')\alpha_{e,o}^{(x)}(\tilde{\mathbf{k}}_1')] = -\frac{1}{2}\mathrm{Im}[t_{e,o}(\mathbf{k}_1')\alpha_{e,o}^{(x)}(\mathbf{k}_1')] + \frac{\sqrt{3}}{2}\mathrm{Im}[t_{e,o}(\mathbf{k}_1')\alpha_{e,o}^{(y)}(\mathbf{k}_1')]. \tag{33}$$

However, in Sec. I E 1 we found that $\mathrm{Im}\left[t_{e,o}(\mathbf{k}_1')\alpha_{e,o}^{(x)}(\mathbf{k}_1')\right] = \sqrt{3}\,\mathrm{Im}\left[t_{e,o}(\mathbf{k}_1')\alpha_{e,o}^{(y)}(\mathbf{k}_1')\right]$, which means that $\mathrm{Im}[t_{e,o}(\tilde{\mathbf{k}}_1')\alpha_{e,o}^{(x)}(\tilde{\mathbf{k}}_1')] = 0$ and from Eq.(12) $\vartheta_{e,o}(\tilde{\mathbf{k}}_1') = 2\pi/3 + m''\pi = (m''+1)\pi - \pi/3$.

F. Discussion of the results of Sec. I E

Similar calculations to those in Sec. I E 1-I E 3 can be performed for all interlayer twist angles $\theta_l = l\pi/6$, $l = 0, 1, 2, \ldots$. We now summarize the most important findings.

- One finds that $\vartheta_{e,o}(\theta_l)$ can be expressed as $\vartheta_{e,o}(\theta_l) = m(\theta_l)\pi - \theta_l$, where $m(\theta_l)$ is an integer.

- The results of Sec. I E 1-I E 3 were obtained for an arbitrary pair of e and o bands. This means, that using Eq. (15) one finds $\vartheta_R(\theta_l) = n(\theta_l)\pi - \theta_l$, where $n(\theta_l)$ is an integer.

- According to Eq. (20), the non-zero matrix elements of H_R^{gr} are $\propto \lambda_R(\theta)e^{\pm i(\theta+\vartheta_R)}$. For $\theta = \theta_l$ one finds that these matrix elements are $\lambda_R(\theta_l)(-1)^{n(\theta_l)}$. This means that for interlayer twist angles where the C_{3v} symmetry of the stack is restored, the Hamiltonian of the induced Rashba SOC simplifies to

$$H_R^{gr} = (-1)^{[n(\theta_l)+1]}\frac{\lambda_R(\theta_l)}{2}\left(\tau_z\sigma_x s_y - \sigma_y s_x\right), \tag{34}$$

  which is, apart from the sign $(-1)^{[n(\theta_l)+1]}$, the well-known result of Refs. [5, 6]. This shows our results are in agreement with general expectations based on the symmetry of the system.

- For twist angles $\theta \in (\theta_l, \theta_{l+1})$, i.e., when the stack has only C_3 symmetry, ϑ_R is a continuous function of θ (through the wavenumbers $\tilde{\mathbf{k}}_j'$). Therefore the matrix elements $\lambda_R(\theta)e^{\pm i(\theta+\vartheta_R)}$ of H_R^{gr} are complex numbers.

- One would expect that $\lambda_R(\theta) = \lambda_R(\theta + 2\pi/3)$. As shown in Figs. 7(b) and 8(b) below, we find that $\lambda_R(\theta) = \lambda_R(\theta + \pi/3)$. Note, that Eq.(1) gives the lowest order non-vanishing contribution. We expect that higher order contributions in the perturbation series, albeit small in magnitude, would lead to $2\pi/3$ periodicity. Note, that $\vartheta_R(\theta) \neq \vartheta_R(\theta + \pi/3) \bmod 2\pi$. This can be seen, e.g., comparing the results of Sec. I E 1 and Sec. I E 3. However, the results of our calculations show that $\vartheta_R(\theta) + \theta$, which gives the phase of the induced Rashba SOC, does change by multiples of 2π upon interlayer rotation by $\theta = \pi/3$.

II. DETAILS OF THE NUMERICAL CALCULATIONS FOR ϑ_R, λ_R AND λ_{vZ}

In this section we discuss questions related to the choice of material and other parameters in our numerical calculations and compare some of our results to corresponding results in Ref. [1].

A. Interlayer tunneling parameters

In Ref. [1] it was argued that for the description of the tunneling between the monolayer graphene (MLG) sheet and the MoS_2 layer it is sufficient to consider only the p orbitals of the chalcogen atoms and one can neglect the d orbitals of the metal atoms. Namely, the the d orbitals are farther away from the carbon atoms of MLG and therefore their overlap with the carbon p_z orbitals should be small. We have extended the calculations of Ref. [1] by taking into account contributions from tunneling processes involving the d orbitals of the metal atoms as well. The results shown in the main text have been obtained in this way.

As already mentioned in Sec. I A, the tunneling matrix $(T(\tau\mathbf{k}'_j))_b$ can be written as

$$\big(T(\tau\boldsymbol{k}'_j)\big)_b = t_b(\tau\mathbf{k}'_j)e^{i\tau\boldsymbol{G}^\theta_j\cdot\boldsymbol{r}_0}\begin{pmatrix} e^{i\tau\phi^A_j} \\ e^{i\tau\phi^B_j}\end{pmatrix}.$$

When only the p orbitals are considered in the interlayer tunneling, then the interlayer tunneling amplitude $t^p_b(\tau\mathbf{K}^\theta,\tau\mathbf{k}'_j)\equiv t^p_b(\tau\mathbf{k}'_j)$ between the $\mathbf{K}^\theta$ point of graphene and electronic states at wavenumber $\mathbf{k}'_j$ in band b of the TMDC is given by

$$t^p_b(\tau\mathbf{k}'_j) = i\tau[c_{bx}(\tau\mathbf{k}'_j)\cos\theta + c_{by}(\tau\mathbf{k}'_j)\sin\theta]\,t^p_{\parallel} + c_{bz}(\tau\mathbf{k}'_j)\,t^p_{\perp}. \tag{35}$$

Here $c_{bx}(\tau\mathbf{k}'_j)$, $c_{by}(\tau\mathbf{k}'_j)$ and $c_{bz}(\tau\mathbf{k}'_j)$ are the complex amplitudes of the p_x, p_y and p_z orbitals of the chalcogen atoms at the BZ point $\mathbf{k}'_j$ in band b of the TMDC. As it was shown in Ref. [1], $t^p_b(\tau\mathbf{k}'_{2,3}) = t^p_b(\tau\mathbf{k}'_1)$. According to Eq. (35), two independent tunneling coefficients are needed: $t^p_{\parallel}$ and $t^p_{\perp}$, and Ref. [1] obtained them from a fitting procedure using previous results [7] of DFT band structures calculations for MLG/TMDC heterostructures. The values of these parameters were estimated to be $t^p_{\parallel}\approx t^p_{\perp}\approx 100\,\mathrm{meV}$.

Considering now the d orbitals of the TMDC metal atoms one can derive a similar expression for the tunneling amplitude $t^d_b(\tau\mathbf{k}'_j)$ between MLG and the d orbitals:

$$\begin{aligned} t^d_b(\tau\mathbf{k}'_{2,3}) = t^d_b(\tau\mathbf{k}'_1) = &\big(c_{b,x^2-y^2}(\tau\boldsymbol{k}'_1)\cos(2\theta) + c_{b,xy}(\tau\boldsymbol{k}'_1)\sin(2\theta)\big)\,t^d_{\square} + \\ &i\tau\left(c_{b,xz}(\tau\boldsymbol{k}'_1)\cos(\theta) + c_{b,yz}(\tau\boldsymbol{k}'_1)\sin(\theta)\right)t^d_{||} + c_{b,3z^2-r^2}(\tau\boldsymbol{k}'_1)t^d_{\perp}. \end{aligned} \tag{36}$$

Here $c_{b,d}(\tau\boldsymbol{k}'_1)$ ($d=\{x^2-y^2,xy,xz,yz,3z^2-r^2\}$) are the complex amplitudes of the d orbitals of the TMDC metal atoms at the BZ point $\mathbf{k}'_1$ in band b. The derivation of Eq(36) involves the same steps as that of Eq. (35) and therefore we do not give further details here. As one can see, $t^d_b(\tau\mathbf{k}'_1)$ involves three more overlap parameters: $t^d_{\square}$, $t^d_{||}$, $t^d_{\perp}$. Therefore there are altogether five $t^{p,d}$ parameters that describe the overlap between graphene's p_z orbitals and the p, d orbitals of the TMDC layer. The approach used in Ref. [1] to estimate $t^p_{\parallel}$ and $t^p_{\perp}$ is not applicable to estimate all five $t^{p,d}$ parameters.

Therefore we used the Slater–Koster method to re-calculate the tunneling coefficients both for the chalcogen p orbitals and the d orbitals of the metal atoms. The steps needed to calculate $t^p_{\parallel}$, $t^p_{\perp}$, $t^d_{\square}$, $t^d_{||}$, and $t^d_{\perp}$ in terms of the set of parameters of the Slater–Koster method are explained in Refs. [1, 4]. We only note that the parametrization of the transfer integrals is based on the Harrison's model[8] and the numerical values of the necessary parameters, with the exception of $\eta_{\mathrm{C-Se}}$, are listed in Ref.[4], see Eqs(4), (5) therein. All our calculations for MLG/MoS_2 are based on the parameters given in Ref.[4].

However, for the calculations for MLG/WSe_2 we also needed the Harrison's model parameter $\eta_{\mathrm{C-Se}}$. We have fixed its value in the following way. We took the values λ_{vZ} and λ_R of the induced valley Zeeman and Rashba SOC from Ref. [7], where they were obtained by fitting band structure calculations of graphene/WSe_2 heterostructures at $\theta=0$ twist angle. Using the methodology of Ref. [1] to calculate λ_{vZ} and λ_R, we adjusted the value of $\eta_{\mathrm{C-Se}}$ such that we obtain a reasonable agreement with Ref. [7], for $\theta=0$. We found that $\eta_{\mathrm{C-Se}}=0.748$ minimizes the deviation to $\approx\pm 20\%$ between our results for λ_{vZ}, λ_R and those of Ref. [7].

To summarize, we used tunneling coefficients shown in Table I. Regarding the t^p coefficients for MoS_2, they are indeed not very different from those estimated in Ref. [1] ($\approx 100\,\mathrm{meV}$) using a different method,

	$t^p_{\parallel}$ [meV]	$t^p_{\perp}$ [meV]	$t^d_{\square}$ [meV]	$t^d_{\parallel}$ [meV]	$t^d_{\perp}$ [meV]
MoS_2	−143.6	144.7	9.2	17.6	−14.9
WSe_2	−76.2	76.2	2.2	4.1	−3.5

TABLE I: Tunneling coefficients

but the sign of $t^p_{||}$ is opposite to the one given in Ref. [1]. This can be traced back to the fact that the TB model of Ref.[9] uses a different orientation of the TMDC lattice with respect to Ref. [1]. This gave rise to an overlooked $\mathbf{k} \to -\mathbf{k}$ transformation in reciprocal space, which resulted in a sign change in the estimation of the tunneling parameter. One can also see that the values of the t^d coefficients are indeed much smaller than $t^p_{\parallel}$ and $t^p_{\perp}$. On the other hand, the complex amplitude factors c_{b,x^2-y^2}, $c_{b,xy}$, $c_{b,xz}$, $c_{b,yz}$, and $c_{b,3z^2-r^2}$ turn out to be significantly larger than c_{bx}, c_{by} and c_{bz} in large regions of the BZ. Therefore $t^d_b(\tau\mathbf{k}'_1)$ is found to be small, but non-negligible with respect to $t^p_b(\tau\mathbf{k}'_1)$.

B. Further parameters

In addition to $t_b(\tau\mathbf{k}'_j)$, there are a couple of further parameters that enter the numerical calculations. We will briefly discuss them here.

- The value of the band gap E_g of the TMDC.

  As briefly discussed in the main text, one can take its value either from experiments (when available) or from previous theoretical works. Regarding the latter, since we use the TMDC TB model of Ref. [9] to calculate the band structure, the spin-orbit coupling Hamiltonian matrix elements and the interlayer tunneling amplitude, we also used the E_g of this model. (We implemented the TB model in the Kwant code[10]). Although the model of Ref. [9] itself is based on DFT calculations, the value of E_g is different from what one can extract from the calculations of Ref. [7] that were performed for MLG/TMDC supercells at $\vartheta = 0$. For example, in the case of MoS_2 the model of Ref. [9] has a band gap that is 17% larger than the corresponding E_g given in Ref. [7]. See Table II for the E_g values used in this work.

- The position of the Dirac point of graphene within the the band gap of the TMDC.

  We describe the energy of the Dirac point of graphene in the band gap of the TMDC by a number $f_G \in [0, 1]$. Its value is a linear function of the position of the Dirac point in the TMDC band gap. When $f_G = 0$, the Dirac point is aligned with the TMDC valence band edge, for $f_G = 1$ the Dirac point has the same energy as the TMDC conduction band edge. When available, the value of f_G can also be taken from experiments[11, 12]. See Table II for the f_g values used in this work.

- The number of bands in the model for the TMDC layer.

  The explicit expression to calculate λ_{vZ} involve a sum over contributions of individual bands. Similarly, in order to calculate ϑ_R and λ_R, one needs to sum over pairs of even (e) and odd (o) bands. Ref. [1] used the approximation that the conduction band (CB) and the valence band (VB) were taken into account for λ_{vZ}, and three pairs of e-o bands for λ_R. As it will be shown below, this already leads to qualitatively good results in most cases, see Sec. II C below. An exception is the value of λ_R for $\theta \approx \pi/6$, where, due to band crossings and near-degeneracies of certain e bands, more pairs of e and o bands need to be taken into account. The TB model that we use involves 11 bands of the TMDC layer. Unless otherwise indicated, we use the contributions of all 11 bands to calculate λ_{vZ}, and 30 pairs of e and o bands for the ϑ_R and λ_R calculations.

	E_g (DFT)	E_g (exp)	f_G (DFT)	f_G (exp)
MoS_2	1.807 eV[9]	2.0 eV[11]	0.974 [7]	0.55[11]
WSe_2	1.638 eV[9]	1.95 eV[12]	0.161[7]	0.426[12]

TABLE II: Band gap and MLG Dirac point energy position parameters from DFT calculation and experiments.

- The TB model of the TMDC

We also note that the TB model of the TMDC appears to be less accurate for the bands above the band gap[9]. This can add further uncertainty to the results, especially in the case graphene/MoS_2, where $f_G = 0.974$, i.e., the relative contributions of e-o band pairs above E_g is larger than the contribution coming from the valence bands.

These details, in addition to those already discussed in Sec. II A, also need to be considered when comparing our results to related previous works[1, 4, 7, 13].

C. Numerical calculations of the induced SOC in MLG/TMDC twisted bilayers

We now show our results for the twist angle dependence of λ_{vZ} and λ_R for graphene/MoS_2 and graphene/WSe_2. In the former case we also compare our results to those of Ref. [1]. For the numerical calculations of λ_R we evaluated Eqs. (13) and (15). To calculate λ_{vZ} we used the result of Ref. [1]:

$$\lambda_{\rm VZ} = 3 \sum_b \frac{|t_b(\boldsymbol{k}_1')|^2 \, \Delta_{0,b}(\boldsymbol{k}_1')}{E_b^2(\boldsymbol{k}_1') - \Delta_{0,b}^2(\boldsymbol{k}_1')}, \tag{37}$$

where $t_b(\boldsymbol{k}_1')$ is defined in Eq. (3) and the summation runs over all bands b of the tight-binding model.

1. *Comparison to the results of Ref. [1]*

First, we briefly discuss how the tunneling parameters shown in Table I modify the results for tunneling amplitude t_b compared to the corresponding results in Ref. [1]. In Fig. 6 we plot the tunneling strength $|t_c|^2$ and $|t_v|^2$ to the CB and VB of MoS_2 as a function of the twist angle θ using the parameters from Table I (solid lines). We also show the corresponding results of Ref. [1], where only $t_\parallel^p \approx t_\perp^p$ were non-zero.

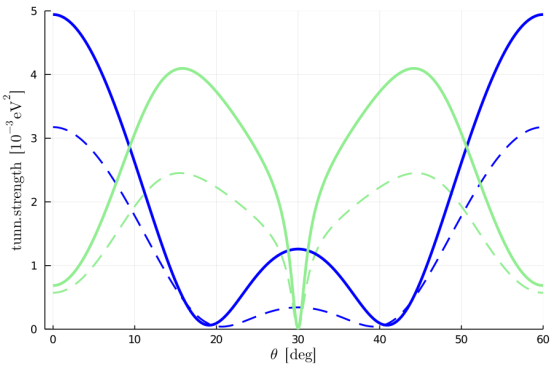

FIG. 6: Tunneling strength $|t_c|^2$ to the conduction band (light green) and to the valence band $|t_v|^2$ (blue) of monolayer MoS_2. The solid curves are the results of this work, the dashed curves are reproduced from Ref. [1].

As one can see in Fig. 6, the present calculations tend to yield larger tunneling strengths. However, the twist angle dependence of $|t_c|^2$ and $|t_v|^2$ remain qualitatively the same.

In Fig. 7(a) we show calculations for λ_{vZ} vs θ for graphene/MoS_2 using the DFT parameters for E_g and f_G, see Table II. The dashed curve in Fig. 7(a) again corresponds to the result of Ref. [1], which uses the contributions of the CB and the VB only. The thin solid line is obtained using the tunneling amplitudes from Table I and only tunneling to the VB and the CB is taken into account. One can see a pronounced increase of $\lambda_{\rm VZ}$ around $\theta = 18°$ with respect to Ref. [1], which is mainly due to the larger tunneling strengths, as shown in Fig. 6. Nevertheless, the curves remain qualitatively very similar. The thick solid line shows the result that we obtain by using the tunneling amplitudes from Table I and taking into account tunneling to all 11 bands of the TB model. It is again qualitatively similar to the other two results, the most important change is the two new zero crossings close to $\theta = 30°$.

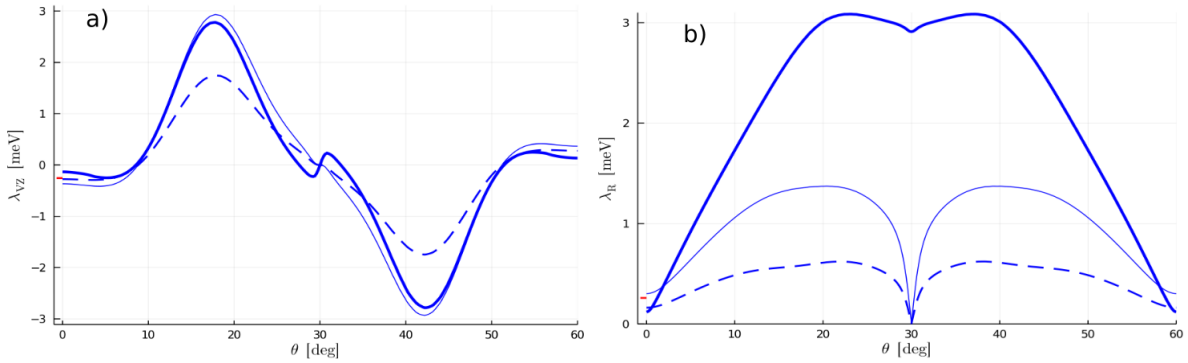

FIG. 7: a) λ_{vZ} and b) λ_R for MLG/MoS_2 as a function of interlayer twist angle θ using the DFT parameters given in Table II. Different lines correspond to different tunneling amplitudes and number of bands in the calculations, see text for details. The red marks at $\theta = 0$ indicate the results of Ref. [7].

In Fig. 7(b) we show similar calculations for λ_R vs θ. The larger tunneling strength t_b used in this work leads again to an enhancement of λ_R (thin solid line) compared to Ref. [1] (dashed line), but the θ dependence of the two results otherwise agree, including the deep minimum at $\theta = 30°$. However, if all possible e-o pairs of bands are included in the calculation (thick solid line), then this minimum becomes a small dip and the value of λ_R is significantly enhanced. As already mentioned, this is because of band crossings and near-degeneracies of certain e bands which means that more pairs of e and o bands need to be taken into account than it was done in Ref. [1].

For comparison, in Fig. 7 we also indicate by red marks the results of the DFT calculations of Ref. [7] for $\theta = 0$. As one can see, all our curves take values close to these reference values. As we explained in Sec. II B, the exact results depend on a number of details, including potentially fine-tuned Slater–Koster parameters. This leaves us with much freedom to adjust our parameters and fit previously published results, but this goes beyond the scope of this paper.

We found a qualitatively similar λ_{vZ} and λ_R vs θ dependence using the experimental parameters of E_g and f_G from Table II, but the maximum values of the induced SOC are significantly smaller.

2. *Calculations for MLG/WSe_2*

Our calculations for the twist angle dependence of λ_{vZ} and λ_R are shown in Fig. 8. We used the tunneling parameters given in Tables I and the DFT parameters in Table II. Contributions from all bands or pairs of bands of the TB model are taken into account. Red marks denote the results of Ref. [7] for $\theta = 0$, they differ $\approx 20\%$ from our results.

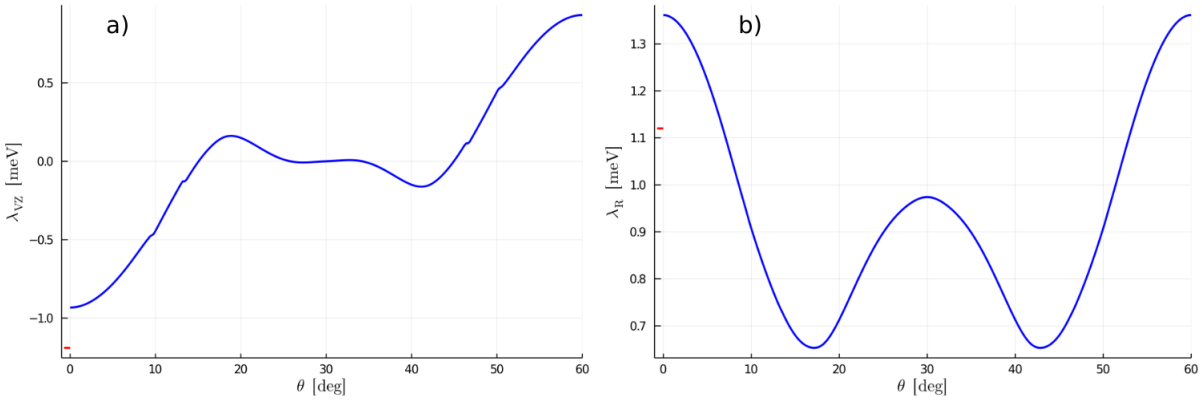

FIG. 8: a) λ_{vZ} and b) λ_R for MLG/WSe_2 as a function of interlayer twist angle θ using the DFT parameters given in Table II. The red marks at $\theta = 0$ indicate the results of Ref. [7].

Importantly, one can see that both $\lambda_{vZ}(\theta)$ and $\lambda_R(\theta)$ are different from the MLG/MoS_2 heterostructures in Fig. 7. This is mainly due to the fact that the Dirac point of graphene is closer to the VB (we used $f_G = 0.161$ in these calculations versus $f_G = 0.976$ in Fig. 7, i.e., here the valence bands give larger contributions. Similarly to MLG/MoS_2, λ_{vZ} and λ_R vs θ dependence using the experimental parameters for E_g and f_G from Table II are qualitatively similar, but the maximum values of the induced SOC are significantly smaller.

Comparison of MLG/MoS_2 and MLG/WSe_2

The different θ dependence of the induced SOC for MLG/MoS_2 (Fig. 7) and MLG/WSe_2 (Fig. 8) explain the differences in the results for the corresponding twisted trilayer systems shown in Fig. 3 of the main text. We point out, in particular, that λ_R has a single maximum for MLG/MoS_2, while it has two maxima for MLG/WSe_2. Together with the θ dependence of ϑ_R given in Fig. 1 of the main text, this can explain the finding that $\lambda_R^{(tls)}$ can be enhanced for WSe_2/MLG/WSe_2, but not for MoS_2/MLG/MoS_2.

3. *Comparison to the results of Refs. [14] and [13]*

During the preparation of this manuscript, a publication by Naimer *et. al.*[14] has appeared discussing the twist angle dependence of the proximity-induced SOC in graphene/TMDC bilayers. Their methodology is based on DFT calculations. The incommensurate graphene/TMDC heterostructures were approximated by periodic supercells, which required several approximations, e.g., straining the graphene sheet.

In agreement with our results, the calculations of Ref. [14] indicate that the strength of the proximity induced SOC in graphene/TMDC heterostructures is tunable by interlayer twist. The twist angle dependence of λ_{vZ} for graphene/MoS_2 and graphene/WSe_2 are qualitatively similar: in the former case there is a maximum at $\theta \approx 20°$, in the latter case λ_{vZ} monotonically decreases as θ is changed from 0° to 30°. They also find that the phase factor ϑ_R in H_R is in general non-zero and depends on the twist angle θ. Regarding the θ dependence of λ_R, for graphene/MoS_2 their result seems to be qualitatively similar to ours, while for graphene/WSe_2 the results show differences. On a more quantitative level, however, our results for λ_{vZ} and λ_R display a much stronger enhancement as a function of θ than in Ref. [14]. The reasons for this discrepancy remains to be investigated in future works.

Another relevant recent work is by Pezo *et. al.*[13], who performed supercell based DFT calculations for graphene/$MoTe_2$ bilayers for three different interlayer twist angles ($\theta = 0, \pi/12, \pi/6$). It was noted in Ref. [13] that the position of graphene's Dirac point is closer to the valence band of $MoTe_2$. Therefore one would expect that the θ dependence of the induced SOC should be similar to the one in graphene/WSe_2, meaning, e.g., that magnitude of both λ_{vZ} and λ_R should decrease for $\theta = \pi/6$ compared to their $\theta = 0$ value. This seems to be in agreement with results of Ref. [13].

Finally, we note that both Refs. [14] and [13] emphasize the effect of the strain that is always present in their supercell based DFT calculations.

III. SUPERMOIRÉ EFFECTS

Let us first consider the moiré effects in a graphene/TMDC system. One can define the primitive moiré wavelength λ_m for a hexagonal heterostructure[15] consisting of graphene and a substrate as

$$\lambda_m = \frac{q}{\sqrt{1+q^2-2q\cos\theta}}\, a_{gr}, \tag{38}$$

where $q = a_s/a_{gr}$ is the ratio of the lattice constants of the substrate (a_s) and of graphene (a_{gr}) and θ is the interlayer twist angle. In the case of graphene and e.g., monolayer MoS_2 this ratio is $q \approx 1.283$. The maximum of λ_m can be found for $\theta = 0$ where $\lambda_m \approx 1.1\,\mathrm{nm}$ (see Fig.9). As a comparison, the moiré length scale is $\lambda_m = 13.9\,\mathrm{nm}$ for a graphene/hBN bilayer at $\theta = 0$.

The moiré potential due to this periodic perturbation leads to, e.g., gap openings at the moiré Brillouin zone boundaries[15] at energies $E_M = \pm\frac{\hbar v_F G_M}{2}$, where $G_M = \frac{4\pi}{\sqrt{3}\lambda_m}$. Using $v_F = 10^6\mathrm{m/s}$, for graphene/MoS_2 this energy scale is $E_M \approx \pm 2.2\mathrm{eV}$ for $\theta = 0$, which is far from the Dirac point. Indeed, in the ARPES experimental results of Ref. [11] on graphene/MoS_2, superlattice effects were observed at binding energies $E_b = -3.55\mathrm{eV}$,

from which the authors concluded that the interlayer twist angle was $\theta \approx 6^\circ$ in their sample. In short, because of the relatively large difference between the graphene and TMDC lattice constants, no moiré effects are to be expected close to the Dirac point of graphene for any twist angle θ in a graphene/TMDC system.

The situation might be different in TMDC/graphene/TMDC trilayers. Namely, studying hBN/graphene/hBN trilayers, Refs. 16 and 17 found that band gaps can appear in the spectrum of these heterostructures at energies closer to the Dirac point of graphene than what was found in hBN/graphene bilayers. This can be understood as a consequence of an interference of the moiré patterns coming from the two hBN layers. Ref. [16] found that if one of the interlayer twist angles, e.g., $\theta^{(b)}$ is kept fixed at $\theta^{(b)} = 0$ and $\theta^{(t)}$ is changed, then the four longest wavelength component $\lambda_{sm}^{(i)}$ of such a *supermoiré* potential in graphene are given by

$$\lambda_{sm}^{(1)} = \frac{q}{\sqrt{2 - 2\cos\theta^{(t)}}}\, a_{gr}, \tag{39a}$$

$$\lambda_{sm}^{(2)} = \frac{q}{\sqrt{(2-\delta)(1-\cos\theta^{(t)}) + \delta^2 - \sqrt{3}\delta\sin\theta^{(t)}}}\, a_{gr}, \tag{39b}$$

$$\lambda_{sm}^{(3)} = \frac{q}{\sqrt{2 - 2\cos\theta^{(t)} + 3\delta^2 - 2\sqrt{3}\delta\sin\theta^{(t)}}}\, a_{gr}, \tag{39c}$$

$$\lambda_{sm}^{(4)} = \frac{q}{\sqrt{(2-\delta)(1-\cos\theta^{(t)}) + \delta^2 + \sqrt{3}\delta\sin\theta^{(t)}}}\, a_{gr}, \tag{39d}$$

where we used the notation $q-1 = \delta$. Eqs. (39) are valid also for TMDC/graphene/TMDC trilayers because the constituent layers have hexagonal lattices. We plot λ_m as well as $\lambda_{sm}^{(i)}$ as a function of $\theta^{(t)}$ using the lattice constants of graphene and MoS_2 in Fig. 9.

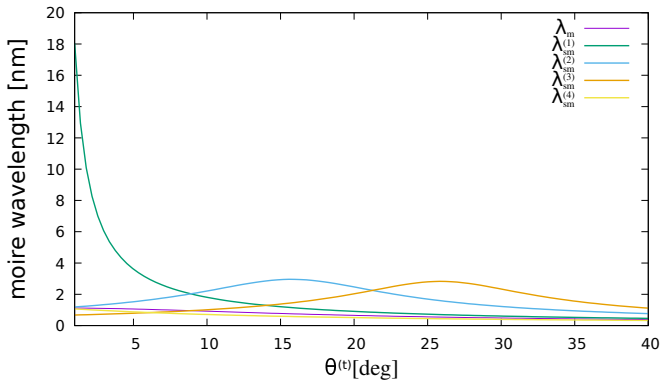

FIG. 9: Moiré wavelength λ_m calculated from Eq. (38) and supermoiré wavelengths calculated from Eqs. (39) as a function of the interlayer twist angle.

As one can see, $\lambda_{sm}^{(2)}$, $\lambda_{sm}^{(3)}$, $\lambda_{sm}^{(4)}$ are always quite short. However, $\lambda_{sm}^{(1)}$ does increase when the two TMDC layers are nearly aligned. For $\theta^{(t)} = 1^\circ$ one finds $\lambda_{sm}^{(1)} = 18$nm corresponding to $E_M = 0.13$eV, which is comparable to the ones found in hBN/Graphene/hBN. Based on these results one may expect an interesting interplay of induced SOC and supermoiré effects in TMDC/graphene/TMDC for $|\theta^{(b)} - \theta^{(t)}| \lesssim 1^\circ$.

IV. MAGNETOTRANSPORT CALCULATIONS FOR GRAPHENE *npn* JUNCTIONS

In this section we briefly explain the theoretical model that was used in the magnetotransport calculations through a *npn* graphene junction with proximity induced SOC shown in Fig. 4 of the main text. We assume that the graphene flake is perfectly ballistic and due to external gates it is doped such that it hosts an *npn* junction, see Fig. 10. We numerically calculate the transmission through the junction as a function of perpendicular magnetic field magnetic field B_z and Fermi energy E_F using the in-house code EQuUs[18].

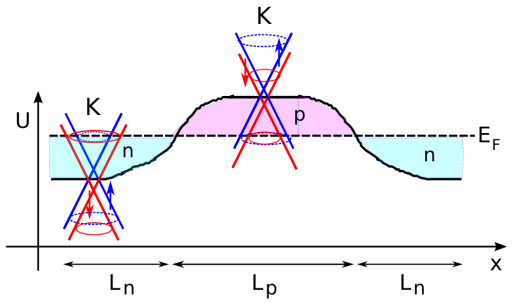

FIG. 10: Schematics of a *npn* junction in graphene. The Dirac point of graphene is shifted in energy due to the doping potential $U(x)$ in the n and p doped regions. The length of the n (p) doped region is L_n(L_p). E_F denotes the Fermi energy.

We use the nearest-neighbor tight-binding (TB) model of graphene:

$$\hat{H}_{orb} = \sum_{i,s} U_i \left(a^\dagger_{i,s} a_{i,s} + b^\dagger_{i,s} b_{i,s} \right) - \gamma \sum_{\langle ij \rangle} e^{\phi_{ij}} a^\dagger_{i,s} b_{j,s} + h.c. \tag{40}$$

where $a^\dagger_{i,s}$ ($a_{i,s}$) and $b^\dagger_{i,s}$ ($b_{i,s}$) are creation (annihilation) operators for electrons of spin s on the A and B sublattice site, respectively. $\gamma = 2.97\,\text{eV}$ is the hopping amplitude between the nearest-neighbor atomic sites $\langle ij \rangle$ in the graphene lattice, ϕ_{ij} encodes the effect of perpendicular magnetic field through Peierls substitution, and U_i is the on-site energy on the atomic site i. Following Ref. [19], we used

$$U(x) = U_n + \frac{U_p - U_n}{2} \left(\tanh\left[\frac{x - L_n}{l_1} \right] - \tanh\left[\frac{x - L_n - L_p}{l_2} \right] \right). \tag{41}$$

Here $L_n = 50\text{nm}$ gives the length of the n-doped regions and we used $U_n = -240\,\text{meV}$. The p-doped middle region was $L_p = 150\,\text{nm}$ long and the doping was $U_p = 40\,\text{meV}$. The parameters $l_1 = l_2 = 25\,\text{nm}$ set the smoothness of the transition between the n and p-doped regions.

In the TB formalism the Bychkov-Rashba SOC can be written as[5, 20]:

$$H_R = i \frac{\lambda_R(\theta)}{3} e^{i \frac{s_z}{2} \vartheta_R} \sum_{\langle i,j \rangle, s, s'} \left[a^\dagger_{i,s} \left(\boldsymbol{s} \times \widehat{\mathbf{d}}_{\langle i,j \rangle} \right)_z b_{j,s'} - h.c. \right] e^{-i \frac{s_z}{2} \vartheta_R} . \tag{42}$$

where $\boldsymbol{s} = (s_x, s_y, s_z)$ are the Pauli matrices representing the electron spin operator. Moreover, $\widehat{\mathbf{d}}_{\langle i,j \rangle} = \mathbf{d}_{\langle i,j \rangle}/d$ are unit vectors, where $\mathbf{d}_{\langle i,j \rangle}$ points from atom j to its nearest neighbors i and $d = |\mathbf{d}_{\langle i,j \rangle}|$. The corresponding continuum SOC Hamiltonian, that can be obtained by Fourier transforming Eq(42) and expanding it at the $\pm K$ points of the Brillouin zone, reads $H_R = \frac{\lambda_R(\theta)}{2} e^{i \frac{s_z}{2} \vartheta_R} \left(\tau_z \sigma_x s_y - \sigma_y s_x \right) e^{-i \frac{s_z}{2} \vartheta_R}$. As long as only a perpendicular magnetic field is applied, the phase ϑ_R will not affect the results, because the corresponding terms in Eq. (42) can be removed by a unitary transformation.

The valley-Zeeman SOC can be written as[20]:

$$H_{vZ} = \frac{i}{3\sqrt{3}} \sum_{\langle\langle i,j \rangle\rangle s,s'} \left[\lambda^{(A)}_{vZ} \nu_{ij} [s_z]_{s,s'} a^\dagger_{i,s} a_{j,s'} + \lambda^{(B)}_{vZ} \nu_{ij} [s_z]_{s,s'} b^\dagger_{i,s} b_{j,s'} \right] . \tag{43}$$

It couples same spins and depends on clockwise ($\nu_{ij} = 1$) or counterclockwise ($\nu_{ij} = -1$) paths along a hexagonal ring from site j to i. In the case of valley-Zeeman SOC $\lambda^{(A)}_{vZ} = -\lambda^{(B)}_{vZ}$. The term Eq.(43) can also describe the intrinsic SOC if the SOC strength λ_I is the same on the two sublattices, i.e., $\lambda^{(A)}_I = \lambda^{(B)}_I$. The corresponding continuum SOC Hamiltonian reads $H_{vZ} = \tau_z s_z \lambda_{vZ}$.

We used periodic boundary conditions perpendicular to the transport direction ($\hat{x}$ in Fig.10). Thus, the transverse momentum q_n is a good quantum number and the total transmission can be calculated as a sum over all q_n:

$$T(E_F, B_z) = \sum_n t(q_n, E_F, B_z) , \tag{44}$$

where $t(q_n, E_F, B_z)$ is the transmission coefficient for mode n. When there are many transverse momenta the exact form of the boundary conditions is not important and therefore we used the infinite mass boundary condition[21] to obtain q_n: $q_n = \left(n + \frac{1}{2}\right) \frac{\pi}{W}$, where $n = 0, 1, 2, \ldots$ and W is the width of the junction.

V. ELECTRON SCATTERING AT A PLANAR JUNCTION IN A GRAPHENE-WSE_2 SYSTEM

We will discuss a further setup to investigate twist-angle dependent transport in a graphene-TMDC system. It is motivated by recent electron optics experiment of Ref.[22, 23] where collimated electron beams were created in monolayer graphene. By making use of such collimated electron beams one can test the twist-angle dependence of the induced SOC through spin-dependent scattering.

To demonstrate this, we consider the TMDC/MLG/TMDC stack shown in Fig. 11. It consists of a MLG/WSe_2 bilayer of a fixed twist angle $\theta^{(b)}$ (purple region). Part of this bilayer is covered by a top WSe_2 layer (orange region) of twist angle $\theta^{(t)}$. Thus the induced SOC in graphene changes at the bilayer-trilayer boundary and in the trilayer region it is assumed to be tunable by $\theta^{(t)}$. The left edge of the top layer defines a junction along the y axis, where ballistic electrons scatter into various forward-propagating and back-propagating modes, as indicated in Fig. 11. We calculate below the reflection coefficient of this junction for a collimated beam of electrons.

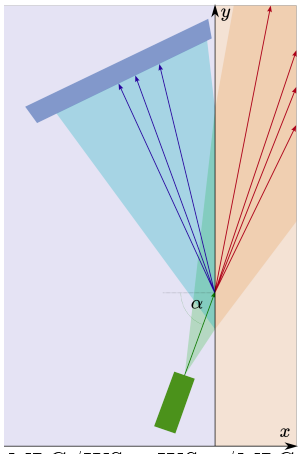

FIG. 11: Ballistic electron scattering in MLG/WSe_2-WSe_2/MLG/WSe_2 junction. The top layer WSe_2 is present only on the right hand side (orange). The electron source produces a collimated beam of 20 meV electrons (green), which scatters into different modes at the junction. Transmitted electrons (red) get absorbed at the far side of the system, while reflected electrons (blue) are absorbed by the drain electrode shown in blue. The reflection coefficient of the junction depends on the rotation angle $\theta^{(t)}$ of the top layer on the right-hand side

The general form of the Hamiltonian is $H^{gr}_{eff} = H^{gr}_{orb} + H^{gr}_{R} + H^{gr}_{vZ}$, see Sec. I D for the definition of each term. On the left-hand side of the junction H^{gr}_{R} is given in Eq. (20), with $\theta = \theta^{(b)}$ and $\lambda_{vZ} = \lambda^{(b)}_{vZ}(\theta^{(b)})$ in H^{gr}_{vZ}. On the right hand side, as shown in the main text, the Rashba Hamiltonian is $H^{(tls)}_{R} = \frac{\lambda^{(tls)}_{R}}{2} e^{i\frac{s_z}{2}\vartheta^{(tls)}} (\tau_z \sigma_x s_y - \sigma_y s_x) e^{-i\frac{s_z}{2}\vartheta^{(tls)}}$, while $\lambda_{vZ} = \lambda^{(b)}_{vZ}(\theta^{(b)}) + \lambda^{(t)}_{vZ}(\theta^{(t)})$ in H^{gr}_{vZ}. One can easily show that the reflection coefficient is the same for electrons in both valleys, for concreteness, we perform the calculation for the K valley. We express the electronic states as plane waves multiplied by spinors in the basis $\{|A\uparrow\rangle, |B\uparrow\rangle, |A\downarrow\rangle, |B\downarrow\rangle\}$ and we assume that their energy is $E = 20$ meV. Due to translational symmetry along $\hat{y}$ axis, the δk_y component of the wavevector of the electronic states is conserved. The SOC leads to the splitting of the bands, therefore (at the E_F given above) for each direction of propagation one can find two modes for the incoming electrons with slightly different wave vectors and opposite pointing spins. We assume a net zero spin polarization with an equal mixture of the two incoming modes, and for each incoming mode, one can find two reflected and two refracted solutions. In total this gives four back-scattered and four forward-scattered modes within one valley. Depending on the exact parameters and the angle of incidence, some of these modes can be decaying waves carrying no current. The particle current operator

can be calculated as $\mathcal{J}_x = \frac{i}{\hbar}[\mathcal{H}, x] = \tau v_F s_0 \otimes \sigma_x$, and in a similar fashion, $\mathcal{J}_y = v_F s_0 \otimes \sigma_y$. The ratio of the current carried by all the back-scattered waves and that of all the incoming modes give us the reflection coefficient:

$$R = -\sum_{i=1}^{4} \langle \mathcal{J}_{x,i}^{(\mathrm{back})} \rangle \Big/ \sum_{i=1}^{2} \langle \mathcal{J}_{x,i}^{(\mathrm{in})} \rangle \ . \tag{45}$$

In an experimental scenario one can never create a beam of electrons with an exact direction of propagation. Nevertheless, as shown in Refs.[22, 23] there are experimental techniques to collimate electrons in graphene from a source. In Ref [22] absorptive pinhole collimators were devised to collimate ballistic electrons into a triangular shaped angular distribution with a half width at half maximum (HWHM) of just below 10°; while in Ref [23] a cosine-shaped distribution was achieved with a similar HWHM of 9° using zigzag contacts to absorb stray electrons. Therefore we consider the effective reflection index $\overline{R}$ that is obtained by averaging R with a certain normalized distribution d centered around an angle of incidence α:

$$\overline{R}(\alpha) = \int d(\alpha' - \alpha) R(\alpha') \mathrm{d}\alpha'. \tag{46}$$

In Fig 12, $\overline{R}$ is plotted as function of the rotation angle $\theta^{(t)}$ of the top TMDC layer for fixed twist angle $\theta^{(b)} = \pi/4$ of the bottom layer. As shown in Fig.2 of the main text, by changing $\theta^{(t)}$ all three SOC parameters $\lambda_R^{(tls)}$, $\vartheta^{(tls)}$ and $\lambda_{vZ}^{(tls)}$ discussed for the trilayer case are changing and they all affect $\overline{R}$. As one can see, the main features in $\overline{R}$ do not seem to depend much on the specific angular distribution of the incoming plane waves or on the exact value of the central angle of incidence.

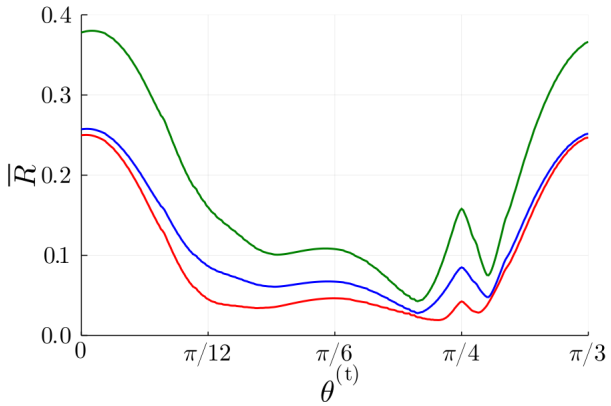

FIG. 12: The effective reflection $\overline{R}$ as a function of $\theta^{(t)}$. Angular distribution of incoming electrons taken from Ref [22] (blue) and from Ref [23] (red) centered at $\alpha = 70°$. The green curve shows the result for $\alpha = 75°$ using the angular distribution from Ref [23].

Experimentally, in order to check the predictions in Fig. 12, a straightforward approach would be to prepare a few different samples with different $\theta^{(t)}$. Alternatively, a setup similar to Ref. [24] could also be feasible, whereby the top layer is rotated *in situ*.

[1] Alessandro David, Péter Rakyta, Andor Kormányos, and Guido Burkard. Induced spin-orbit coupling in twisted graphene–transition metal dichalcogenide heterobilayers: Twistronics meets spintronics. *Phys. Rev. B*, 100(8):085412, August 2019.

[2] Andor Kormányos, Viktor Zólyomi, Neil D. Drummond, and Guido Burkard. Spin-Orbit Coupling, Quantum Dots, and Qubits in Monolayer Transition Metal Dichalcogenides. *Phys. Rev. X*, 4(1):011034, March 2014.

[3] M. S Dresselhaus, G Dresselhaus, and A Jorio. *Group theory: application to the physics of condensed matter*. Springer-Verlag, Berlin, 2010. OCLC: 692760083.

[4] Yang Li and Mikito Koshino. Twist-angle dependence of the proximity spin-orbit coupling in graphene on transition-metal dichalcogenides. *Phys. Rev. B*, 99(7):075438, February 2019. Publisher: American Physical Society.

[5] C. L. Kane and E. J. Mele. Quantum Spin Hall Effect in Graphene. *Phys. Rev. Lett.*, 95(22):226801, November 2005.

[6] Hongki Min, J. E. Hill, N. A. Sinitsyn, B. R. Sahu, Leonard Kleinman, and A. H. MacDonald. Intrinsic and Rashba spin-orbit interactions in graphene sheets. *Phys. Rev. B*, 74(16):165310, October 2006.

[7] Martin Gmitra, Denis Kochan, Petra Högl, and Jaroslav Fabian. Trivial and inverted Dirac bands and the emergence of quantum spin Hall states in graphene on transition-metal dichalcogenides. *Phys. Rev. B*, 93(15):155104, April 2016. Publisher: American Physical Society.

[8] Walter Ashley Harrison. *Elementary Electronic Structure*. World Scientific, 1999. Google-Books-ID: eAfi3ajSTcUC.

[9] Shiang Fang, Rodrick Kuate Defo, Sharmila N. Shirodkar, Simon Lieu, Georgios A. Tritsaris, and Efthimios Kaxiras. Ab initio tight-binding Hamiltonian for transition metal dichalcogenides. *Phys. Rev. B*, 92(20):205108, November 2015. Publisher: American Physical Society.

[10] Christoph W. Groth, Michael Wimmer, Anton R. Akhmerov, and Xavier Waintal. Kwant: a software package for quantum transport. *New J. Phys.*, 16(6):063065, June 2014. Publisher: IOP Publishing.

[11] Debora Pierucci, Hugo Henck, Jose Avila, Adrian Balan, Carl H. Naylor, Gilles Patriarche, Yannick J. Dappe, Mathieu G. Silly, Fausto Sirotti, A. T. Charlie Johnson, Maria C. Asensio, and Abdelkarim Ouerghi. Band Alignment and Minigaps in Monolayer MoS $_2$ -Graphene van der Waals Heterostructures. *Nano Letters*, 16(7):4054–4061, July 2016.

[12] H. Nakamura, A. Mohammed, Ph. Rosenzweig, K. Matsuda, K. Nowakowski, K. Küster, P. Wochner, S. Ibrahimkutty, U. Wedig, H. Hussain, J. Rawle, C. Nicklin, B. Stuhlhofer, G. Cristiani, G. Logvenov, H. Takagi, and U. Starke. Spin splitting and strain in epitaxial monolayer WSe_2 on graphene. *Phys. Rev. B*, 101:165103, Apr 2020.

[13] Armando Pezo, Zeila Zanolli, Nils Wittemeier, Adalberto Fazzio, Stephan Roche, and Jose H. Garcia. A twist for tuning the spin-orbit coupling in graphene/transition metal dichalcogenide heterobilayers. *arXiv:2011.06714*, 2020.

[14] Thomas Naimer, Klaus Zollner, Martin Gmitra, and Jaroslav Fabian. Twist-angle dependent proximity induced spin-orbit coupling in graphene/transition metal dichalcogenide heterostructures. *Phys. Rev. B*, 104:195156, Nov 2021.

[15] Matthew Yankowitz, Jiamin Xue, Daniel Cormode, Javier D. Sanchez-Yamagishi, K. Watanabe, T. Taniguchi, Pablo Jarillo-Herrero, Philippe Jacquod, and Brian J. LeRoy. Emergence of superlattice dirac points in graphene on hexagonal boron nitride. *Nature Physics*, 8(5):382–386, May 2012.

[16] Miša Andjelković, Slaviša P. Milovanović, Lucian Covaci, and François M. Peeters. Double moiré with a twist: Supermoiré in encapsulated graphene. *Nano Letters*, 20(2):979–988, 2020. PMID: 31961161.

[17] Hiroki Oka and Mikito Koshino. Fractal energy gaps and topological invariants in hbn/graphene/hbn double moiré systems. *Phys. Rev. B*, 104:035306, Jul 2021.

[18] Eötvös Quantum Utilities.

[19] G. Nanda, J. L. Aguilera-Servin, P. Rakyta, A. Kormányos, R. Kleiner, D. Koelle, K. Watanabe, T. Taniguchi, L. M. K. Vandersypen, and S. Goswami. Current-phase relation of ballistic graphene josephson junctions. *Nano Letters*, 17(6):3396–3401, 2017.

[20] Tobias Frank, Petra Högl, Martin Gmitra, Denis Kochan, and Jaroslav Fabian. Protected Pseudohelical Edge States in Z_2-Trivial Proximitized Graphene. *Phys. Rev. Lett.*, 120(15):156402, April 2018.

[21] A. R. Akhmerov and C. W. J. Beenakker. Boundary conditions for dirac fermions on a terminated honeycomb lattice. *Phys. Rev. B*, 77:085423, Feb 2008.

[22] Arthur W. Barnard, Alex Hughes, Aaron L. Sharpe, Kenji Watanabe, Takashi Taniguchi, and David Goldhaber-Gordon. Absorptive pinhole collimators for ballistic Dirac fermions in graphene. *Nature Communications*, 8(1):15418, May 2017. Number: 1 Publisher: Nature Publishing Group.

[23] S. Bhandari, G. H. Lee, K. Watanabe, T. Taniguchi, P. Kim, and R. M. Westervelt. Imaging electron flow from collimating contacts in graphene. *2D Mater.*, 5(2):021003, March 2018. Publisher: IOP Publishing.

[24] Rebeca Ribeiro-Palau, Changjian Zhang, Kenji Watanabe, Takashi Taniguchi, James Hone, and Cory R. Dean. Twistable electronics with dynamically rotatable heterostructures. *Science*, 361(6403):690–693, August 2018.